Chemical Science

EDGE ARTICLE

View Article Online
View Journal | View Issue

Check for updates

Cite this: Chem. Sci., 2023, 14, 9704

All publication charges for this article have been paid for by the Royal Society of Chemistry

Understanding C–H activation in light alkanes over Cu-MOR zeolites by coupling advanced spectroscopy and temperature-programmed reduction experiments†

Karoline Kvande,[a] Beatrice Garetto,[b] Gabriele Deplano,[b] Matteo Signorile,[b] Bjørn Gading Solemsli,[a] Sebastian Prodinger,[a] Unni Olsbye,[a] Pablo Beato,[c] Silvia Bordiga,[b] Stian Svelle*[a] and Elisa Borfecchia*[b]

Received 31st March 2023
Accepted 19th August 2023

DOI: 10.1039/d3sc01677c

rsc.li/chemical-science

The direct activation of methane to methanol (MTM) proceeds through a chemical-looping process over Cu-oxo sites in zeolites. Herein, we extend the overall understanding of oxidation reactions over metal-oxo sites and C–H activation reactions by pinpointing the evolution of Cu species during reduction. To do so, a set of temperature-programmed reduction experiments were performed with CH_4, C_2H_6, and CO. With a temperature ramp, the Cu reduction could be accelerated to detect changes in Cu speciation that are normally not detected due to the slow CH_4 adsorption/interaction during MTM (~200 °C). To follow the Cu-speciation with the three reductants, X-ray absorption spectroscopy (XAS), UV-vis and FT-IR spectroscopy were applied. Multivariate curve resolution alternating least-square (MCR-ALS) analysis was used to resolve the time-dependent concentration profiles of pure Cu components in the X-ray absorption near edge structure (XANES) spectra. Within the large datasets, as many as six different Cu^{II} and Cu^{I} components were found. Close correlations were found between the XANES-derived Cu^{II} to Cu^{I} reduction, CH_4 consumption, and CO_2 production. A reducibility–activity relationship was also observed for the Cu-MOR zeolites. Extended X-ray absorption fine structure (EXAFS) spectra for the pure Cu components were furthermore obtained with MCR-ALS analysis. With wavelet transform (WT) analysis of the EXAFS spectra, we were able to resolve the atomic speciation at different radial distances from Cu (up to about 4 Å). These results indicate that all the Cu^{II} components consist of multimeric Cu^{II}-oxo sites, albeit with different Cu–Cu distances.

1 Introduction

Methane, being the principal component of natural gas, is a vastly underutilized raw material for the chemical industry.[1] Due to the strong C–H bond in light alkanes, one of the biggest challenges to overcome is the over-oxidation of the desired products. Therefore, extensive research efforts have been devoted to reaction design and material development to find direct reaction routes that can overcome the issue of over-oxidation.[2,3] These approaches involve the direct activation of methane-to-methanol. A high selectivity toward methanol has been obtained in a direct reaction route, albeit at the expense of a high yield. One of the more promising methods to obtain a high selectivity has been through a cyclic, stepwise reaction process where both products and reactants are kept separate with the aid of Cu-loaded zeolites that form Cu_xO_y-moieties when exposed to oxygen at high temperatures (~500 °C).[4] In the second step, at lower temperatures (~200 °C), the Cu_xO_y-moieties are exposed to CH_4 leading to the reduction of some of the Cu-oxo sites and the formation of methoxy intermediates. In the final step, steam is introduced to extract methanol as the product. To increase the output of the reaction, while maintaining the selectivity, fine-tuning of reaction protocols and optimization of materials are essential.[3,5] Consequently, the effect of Cu speciation, material properties, and reaction mechanism need to be unfolded and understood. Learning more about these properties would also potentially open the doors to other oxidation reactions and C–H activation routes.

Over the years, many zeolite systems have been studied, where the more active ones are MOR,[6–11] CHA,[12,13] FER,[14] FAU,[15] and MAZ.[16] The mentioned zeolites feature a combination of large and small ring systems, rendering it difficult to determine which zeolite properties are most important for methane

---

[a] Centre for Materials Science and Nanotechnology (SMN), Department of Chemistry, University of Oslo, 1033 Blindern, 0315, Oslo, Norway. E-mail: stian.svelle@kjemi.uio.no

[b] Department of Chemistry, NIS Center and INSTM Reference Center, University of Turin, 10125 Turin, Via P. Giuria 7, Italy. E-mail: elisa.borfecchia@unito.it

[c] Topsoe A/S, Haldor Topsøes Allé 1, DK-2800 Kgs. Lyngby, Denmark

† Electronic supplementary information (ESI) available. See DOI: https://doi.org/10.1039/d3sc01677c

activation and methanol formation. However, well-distributed Cu ions,[17] as well as an intermediate loading of Cu have been identified as important requirements to achieve the highest methanol yields.[10,18] This is linked with the need to have Cu ions in suitable proximity to form both accessible and reducible multimeric species, while at the same time retaining a sufficient number of Brønsted acid sites to effectively aid in stabilizing the intermediates.[19] Both monomeric,[12,20] dimeric,[18,21] and trimeric[11,22] copper species have been proposed as the active sites,[11,22] however, a redox mechanism involving mixed Cu^{II}/Cu^{I} sites in dimeric Cu_xO_y-moieties, *e.g.* mono-μ-oxo dicopper(II), does seem to best meet the criterion of the two-electron process of converting methane to methanol.[18,21,23,24]

There are still many unanswered questions regarding the changes to the Cu_xO_y-sites upon CH_4 activation, H_2O extraction, and subsequent reoxidation. Thus far, the literature indicates that CH_4 activation proceeds *via* the formation of methoxy intermediates upon interaction with the Cu-sites that are stabilized on either Cu species or Brønsted acid sites nearby.[25,26] Then, for the methanol formation, several groups have recently suggested a mechanism where the role of H_2O is not only to displace the products but also to be the main oxygen donor.[27–29] It is, however, well established that activation in O_2 at high temperature leads to a fully oxidized Cu^{II} state of the zeolite. Further, it has been demonstrated that a fraction of the Cu^{II} is reduced to Cu^{I} when CH_4 is introduced at *e.g.* 200 °C. However, only a fraction of the Cu^{II} is reduced, often around 30%.[6,7,11,12,21,23] Upon introduction of H_2O for the extraction of methanol, hydrolysis of Cu species have been reported, followed by a slow reoxidation of Cu^{I} back to Cu^{II}.[23]

Many different experimental and computational methods have been used to clarify the mechanism and pinpoint performance descriptors, as the stepwise nature of the reaction makes it very difficult to obtain kinetically relevant information.[19,30] A potentially relevant method for the reaction is temperature-programmed reduction (TPR) with CH_4. In a recent work by Sushkevich *et al.*, they showed by comparing different zeolite topologies that FAU zeolites needed a higher CH_4-loading temperature for the Cu_xO_y-sites to be active towards methanol formation.[15] Similarly, Kvande *et al.* relied on CH_4-TPR to show that SAPO-34 needed a higher C–H activation temperature than the isostructural CHA zeolite, SSZ-13, to increase the methanol yield. This was associated with dissimilar Cu-sites or lattice components in the two CHA-type frameworks.[31] As both of these previous studies compare different zeolite topologies, we found it intriguing to determine if CH_4-TPR also could elucidate differences within the same zeolite system, but with different composition and MTM activity, to find relationships between structure/reducibility and activity. To that end, we chose two MOR zeolites with different Si/Al and Cu/Al ratio, well-characterized from several previous studies.[18,23,32–34] To follow the Cu-speciation throughout the TPR protocol and connect CH_4 oxidation to Cu reduction, we have coupled the TPR experiment with *in situ* X-ray absorption spectroscopy (XAS). Multivariate curve resolution alternating-least-square (MCR-ALS) analysis was performed to obtain the spectral signatures of pure Cu species contributing to the Cu K-edge X-ray absorption near edge structure (XANES) signal as well as their time/temperature-dependent concentration profiles. This is a technique that has given impressive, value-added input to understand the Cu-speciation in zeolites.[35,36] Martini *et al.* used MCR-ALS analysis to identify differences in the Cu-speciation in a Cu-CHA when exposed to O_2 or He during activation and was able to connect this with the reducibility of the samples.[35] In another work by Pappas *et al.* on the same Cu-MOR investigated herein, it was shown with MCR-ALS analysis on high energy resolution fluorescence-detected (HERFD) XANES that two different framework-coordinated Cu^{II} species form at high temperatures.[18] One of these species was linked to the Cu^{II} active site in Cu-MOR for MTM. To enhance our understanding of the Cu reducibility and broaden the applicability of our findings, C_2H_6 and CO were also employed as substrates/reductants in the TPR protocol, while probing the sample response by *in situ* XAS. C_2H_6-TPR was performed to deepen and expand our understanding of C–H activation in light hydrocarbons over Cu-zeolites beyond the iconic CH_4 case. This is important since ethane, although much less abundant than methane, is the second largest component of natural gas, and there are large repositories of underutilized natural gas, especially from the abundant shale gas reserves. The industrially applied method for converting ethane is *via* steam cracking, which is a very energy intensive method leading to a high fraction of CO_2.[37] It is therefore important to find alternative pathways for converting ethane, where some suggested approaches thus far has involved oxidative and non-oxidative dehydrogenation of ethane to ethylene, aromatization, ammoxidation and also partial oxidation.[29] In parallel, CO adsorption/desorption experiments on Cu-zeolites have been widely used to shed light on Cu-speciation and accessibility.[32,38–41] Notably, CO also represents a possible over-oxidation product in MTM schemes, and low-temperature dry CO oxidation to CO_2 has been proposed as an effective probe reaction to assess the presence of multimeric Cu_xO_y-moieties in zeolites.[42–44] For all these reasons, CO-TPR studies were performed, under comparable *in situ* conditions.

In addition to XANES, also the longer energy range corresponding to extended X-ray absorption fine structure (EXAFS) was collected and included in the MCR-ALS analysis,[45] allowing us to extract and analyze EXAFS spectra of the pure Cu components. An innovative approach, linking each pure EXAFS spectrum to an average temperature based on the MCR concentration profiles is implemented, to account for the inherent temperature dependence of the EXAFS signal in the interpretation of the results. Finally, Wavelet Transform (WT) analysis was used to untangle the different scattering contributions shaping the high-*R* region of the EXAFS spectra,[34] thus providing unambiguous evidence for the nuclearity of the pure Cu-species formed in the MOR lattice. *In situ* XAS results are correlated with the CO_2 formation and reactant consumption profiles obtained from Mass Spectrometry (MS) analysis and combined with complementary insights from Diffuse Reflectance ultraviolet-visible (UV-vis) and Fourier-transform infrared (FT-IR) spectroscopies.

2 Methods

2.1 Material properties

The two Cu-exchanged mordenites investigated herein were prepared from commercially obtained zeolites from Zeolyst. The 018Cu-MOR(7) was prepared from CBV10ADS (Na-MOR, Si/Al = 7) and the 036Cu-MOR(11) from CBV21A (NH_4-MOR, Si/Al = 11). The zeolites were exchanged into their proton form before Cu-loading. The preparation and physicochemical characterization (scanning electron microscopy (SEM), energy dispersive X-ray (EDX) analysis, and powder X-ray diffraction (XRD)) of the materials have been described in detail in previous work from our group.[18,33] The samples have also been subjected previously to an array of more advanced characterization involving CO-adsorption with FT-IR spectroscopy, XAS, X-ray photoelectron spectroscopy (XPS), and magic angle spinning (MAS) NMR spectroscopy.[18,32,33,46] The sample nomenclature is given as [Cu/Al]Cu-MOR([Si/Al]). The Cu/Al, Si/Al, and Cu concentration (in μmol g^{-1}) as measured by EDX are reported in Table 1. Also, the activity of the materials in the methane-to-methanol reaction from fixed-bed laboratory tests under optimized conditions is reported in Table 1. The values were first reported by Dyballa *et al.*[33]

2.2 *In situ* XAS temperature-programmed reduction (TPR) experiments with CH_4, C_2H_6, and CO

TPR experiments were conducted in thin capillary reactors simultaneously as X-ray absorption spectra were collected. About 6 mg of sample were pressed and sieved (160–125 μm) and placed into a quartz capillary (1.5 mm i.d. and 0.01 mm thickness) with a quartz wool plug at each end of the bed. The capillary was then glued to a special-designed bracket so that gas could flow through. The capillary was heated with a heat blower placed directly under the reactor bed. The temperature set points were calibrated with a thermocouple placed inside an empty capillary before the experiments. Three mass flow controllers (MFCs) together with automatic 4-way valves (kept at 120 °C to remove traces of moisture) were used to control the flows of He (100%), O_2 (100%), and either CH_4 (2%/rest. He), C_2H_6 (3%/rest. He), or CO (5%/rest. He). All flows were set to 5 ml min^{-1}, and the effluent was analyzed with an online MS. The reaction protocol is depicted in Scheme 1. Before the TPR ramp, the samples were heated to 500 °C in O_2 and kept in these conditions for 2 h before it was first cooled (10 °C min^{-1}) to 200 °C and subjected to He for 30 min to clean away possible contaminants when switching the automatic 4-way valve between O_2 and He. Then the samples were cooled further to 120 °C and kept in inert treatment for 1 h before being exposed to the reducing agent. After reaching a steady trace (~20 min) in the MS, the samples were heated at 5 °C min^{-1} up to 550 °C.

The Cu K-edge *in situ* XAS data were collected in transmission mode on the BM31 beamline of the European Synchrotron Radiation Facility (ESRF, Grenoble, France).[47] The beamline was equipped with a water-cooled double-crystal monochromator (flat Si[111] pair) and ionization chambers, filled with a He/Ar mixture, were used for the detection of the incident (I_0) and transmitted photons (I_1).[48] All the XAS spectra were collected with an acquisition time of *ca.* 3 min per scan. The obtained data were normalized to unity edge jump at the Cu K-edge by the Athena software from the Demeter suite.[49]

2.3 *In situ* ultraviolet-visible (UV-vis) spectroscopy of CH_4-TPR experiments

Supporting CH_4-TPR experiments coupled with UV-vis were performed on a purpose-designed test rig for *in situ* and *operando* UV-vis gas-phase experiments, where the probe is placed into the middle of an oven, touching the tubular quartz reactor (9 mm i.d.) perpendicular to the reactor bed. About 100 mg of pressed and sieved (500–250 μm) sample was prepared and placed inside the quartz reactor on a glass wool plug. The temperature was controlled by a thermocouple touching the pelletized sample bed. The spectra were recorded in reflectance (%) mode on an Avantes AvaSpec-ULS2048XL-EVO fiber optics spectrometer (100 μm slits) with an Avantes AvaLight-DH-S light source (including both a deuterium and a halogen lamp). For the collection of diffuse reflected light from the sample, a custom high-temperature resistant fiber optic with a high-OH fused silica core (diameter = 100 μm) was used. Polytetrafluoroethylene (PTFE) powder was measured at room temperature (RT) as a 100% reflectance reference before the TPR experiments. The same protocol as reported in Scheme 1 was followed. For the ramp, a flow of 15 ml min^{-1} CH_4 (20%/rest. He) was applied. UV-vis spectra were collected continuously at all steps of the protocol. For the TPR ramp, one spectrum, obtained as the average of 50 scans with 10 ms integration time each, was collected every 50 s.

2.4 Multivariate curve resolution-alternating least squares (MCR-ALS) analysis of *in situ* XAS data

XAS uniquely gives access to local structural information without any need for long-range order in the Cu sites distribution.[50,51] However, in the presence of different Cu species in the zeolite, the technique provides an average signal over all the Cu sites in the mixture. In this regard, Multivariate Curve

Table 1 Relevant elemental composition and MTM performance results of the Cu-MOR samples

Sample	Cu/Al	Si/Al	Cu (μmol g^{-1})	MTM[a] yield (μmol_{MeOH} g^{-1})	MTM[a] productivity (mol_{MeOH} mol_{Cu}^{-1})
018Cu-MOR(7)	0.18	7	367	172	0.47
036Cu-MOR(11)	0.36	11	500	124	0.25

[a] MTM yield and productivity as previously reported.[33]

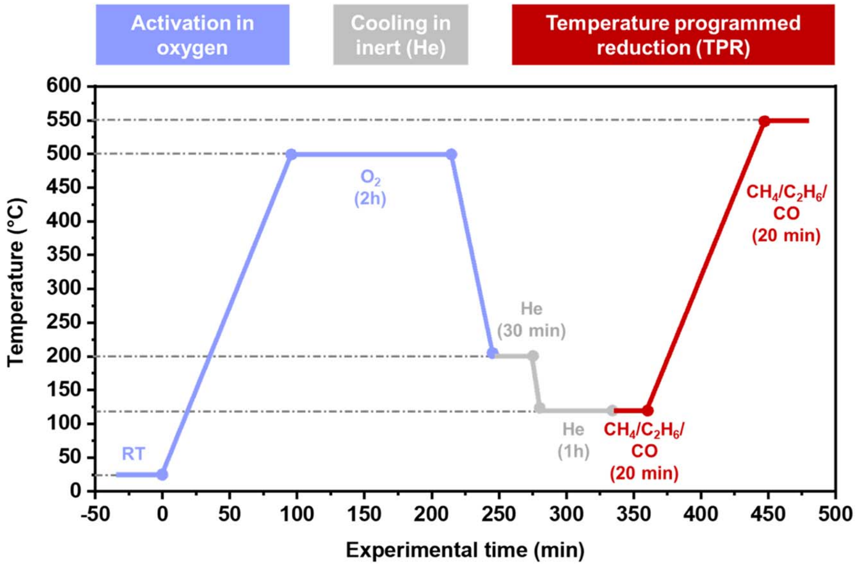

Scheme 1 Experimental protocol for *in situ* XAS during TPR experiments over Cu-MOR samples. The protocol consists of activation in oxygen at 500 °C, followed by two cooling steps. First, the sample was cooled in oxygen until 200 °C before a second cooling step to 120 °C in inert (He). Then the samples were exposed to a reductive atmosphere (either CH_4, C_2H_6, or CO) while the temperature was ramped up (5 °C min^{-1}) to 550 °C.

Resolution-Alternating Least Squares (MCR-ALS) analysis represents a powerful method to deepen the characterization, by resolving individual contributions from pure Cu species. MCR-ALS allows the decomposition of an experimental matrix $\boldsymbol{D}$ into pure contributions, such as spectra $\boldsymbol{S}$ matrix and the corresponding concentration profile $\boldsymbol{C}$ matrix: $\boldsymbol{D} = \boldsymbol{C}\cdot\boldsymbol{S}^T$. Initially, the number of principal components (PCs) must be determined following a critical assessment of the results in terms of spectroscopic and chemical–physical meaningfulness.[52–54] The principal results that MCR-ALS returns are concentration profiles and spectra of pure components. The generation of the pure components is performed by initial guesses efficiently managed by specific methods, such as SIMPLISMA.[55]

In the present work, the whole experimental energy range (8800–9727 eV), including both the XANES and the EXAFS spectral regions, of normalized and energy-aligned XAS spectra was analyzed by MCR-ALS. The normalized $\mu(E)$ XAS spectra, starting from the pretreatment step under static conditions in O_2 at 500 °C, were organized in three datasets according to the reducing agent used during the TPR step, joining the datasets related to the two investigated Cu-MOR samples. MCR-ALS reconstruction was carried out using the MATLAB-based MCR-ALS Graphical User Interface (GUI) developed by Jaumot *et al.*, using Matlab R2022a.[56] For further details on the specific method implementation and the ALS quality control parameters, the interested reader is referred to ESI, Section S2 and S3.†

2.5 Wavelet transform (WT) EXAFS analysis

Fourier-Transform (FT-)EXAFS analysis is traditionally employed to access detailed information about the local structure and coordination environment around a specific metal center.[57] However, when different neighboring atoms are localized at similar distances around the absorber, their scattering contributions can overlap in *R* space, becoming indistinguishable.[58,59] In the present case, such overlap issues are especially present in the 2.5–3.5 Å range, involving framework T atoms (Si, Al) and Cu atoms from multimeric Cu-species formed in Cu-MOR at high-temperature treatment in O_2. A possible solution to overcome this problem is to associate the conventional FT-EXAFS to its *k*-space EXAFS signal, thus enhancing the sensitivity to the chemical nature of the scatterer by exploiting the scatterer Z-dependency in the backscattering amplitude functions, $F(k)$.[60,61] This task can be performed by an innovative spectral processing technique called Wavelet Transform (WT) analysis. With this technique, a 2D representation of the EXAFS, showing *k*- and *R*-space spectral features simultaneously is possible.[57] The mother function that is used to obtain the WTs maps and the related power density functions is the so-called Morlet function:

$$\psi(k) = \frac{1}{\sqrt{2\pi}\sigma}\, e^{i\eta k}\, e^{-\frac{k^2}{2\sigma^2}} \tag{1}$$

where i denotes the complex unit, and η indicates the frequency of a sine wave convoluted by a Gaussian curve with σ as the standard deviation.[34] The selected values of the η and σ parameters regulate the resolution in *R* and *k* space, allowing the operator to achieve the best visualization of the desired spectral features.[62] In this regard, knowing that the typical Cu–Cu distance in dicopper(II)-oxo species formed in zeolites falls in the 3–4 Å range (average values of 3.5 Å), the best resolution condition at a given distance of interest is obtained choosing $\sigma = 1$ and $\eta = 7$ for all the WT representations.[60,63,64]

To more easily compare different spectra, focusing on the presence and properties of Cu–Cu contributions, the so-called power density function $\Phi^R(k)$ of the WT representation was also calculated.[34,65] This function represents integrals of the squared modulus of the WT over the R-space range of interest, according to the following definition:

$$\Phi^R(k) = \int_{R_{\min}}^{R_{\max}} \mathrm{d}R' \left| W_{\chi}{}^{\psi}(k, R') \right|^2 \tag{2}$$

where $W^{\psi}(k,R)$ is the WT representation of the EXAFS signal using the mother function ψ, and the integral is computed from $R_{\min}$ to $R_{\max}$, here set to 2.5 and 4.0 Å respectively.

2.6 *In situ* Fourier transform infrared (FT-IR) spectroscopy of CO-TPR and desorption experiments

The CO-TPR experiment was conducted on a Bruker Vertex 80 instrument equipped with a Mercury–Cadmium-Telluride (MCT) detector cooled with liquid nitrogen. The material was pressed into a thin, self-supporting wafer (7.5 mg cm^{-2}) and placed inside an AABSPEC cell with low free volume (model #CXX), where both temperature and gas flow can be controlled. For the TPR experiment, the sample was heated to 500 °C (5 °C min^{-1}) in a flow of O_2 (100%), before being cooled down to 120 °C (10 °C min^{-1}), where He (100%) was purged on the sample for 1 h. Then, the gas flow was switched to CO (10%/rest. He) and ramped up to 500 °C (10 °C min^{-1}). A spectrum was collected every 40 s. To calculate the CO concentration (in μmol g^{-1}), the following form of Lambert–Beer law was applied:

$$A = \varepsilon \times C \times \rho \tag{3}$$

where A (cm^{-1}) is the integrated absorbance defined in a specific spectral region, ρ (mg cm^{-2}) is the pellet density, ε (cm μmol^{-1}) is the molar attenuation coefficient (11.5 cm μmol^{-1}) obtained from Deplano *et al.*,[40] and C (μmol g^{-1}) is the concentration of CO.

3 Results

3.1 *In situ* XANES of Cu-MOR during CH_4, C_2H_6 and CO-TPR: a qualitative overview

Two MOR zeolites, 036Cu-MOR(11) and 018Cu-MOR(7), with different compositions and MTM activity (Table 1), were subjected to three different TPR experiments. By following the protocol presented in Scheme 1, CH_4, C_2H_6, and CO-TPR were performed. XAS spectra were collected throughout the entire experiment. The Cu K-edge XANES spectra collected during pretreatment in O_2 and subsequent cooling step are reported in the ESI, Section S1.† Before O_2 activation, in the as-prepared Cu-MOR zeolites, Cu ions mostly occurred as mobile hydrated Cu^{II} complexes.[11,18] Then, as expected, during the high-temperature activation step in O_2, the Cu ions progressively turned into framework-coordinated Cu^{II} species with three/four-fold coordination.[46,66] When cooling from 500 to 120 °C, the Cu^{II} oxidation state is fully preserved. Small modifications in the spectral shape are observed and are suggested to stem from temperature-dependent rearrangements in the coordination motif for a small fraction of framework-coordinated Cu ions. This has already been observed for Cu-MOR under equivalent conditions.[23,46] Fig. 1 reports the XANES spectra obtained during the TPR protocol for the three different reducing atmospheres (CH_4, C_2H_6, and CO). In all cases, the reduction of Cu is visible. Spectroscopically, this is indicated by the progressive decrease of the pre-edge peak at 8977 eV related to the 1s → 3d transition in Cu^{II} ions (see ESI, Section S1† for further details), paralleled by the development of a prominent Cu^{I} 1s → 4p rising-edge peak located at *ca.* 8983 eV.[61] The intensity loss in the white line (WL) peak region indicates a decrease in the average coordination number of the absorber.[67] This is consistent with the progressive formation of linear or quasi-linear Cu^{I} species.[23]

During the reduction in CO, qualitative XAS analysis suggests a more complex reaction pathway. The appearance of an intermediate Cu^{I} species is detected in the XANES spectra and highlighted by the black boxes in Fig. 1, right panels. The characteristics of this species will be discussed in the following, based on MCR-ALS results. At the end of the TPR protocols (550 °C), signals related to characteristic Cu^{II} transitions are no longer visible in any of the experiments. Based on this, we qualitatively confirm that a virtually pure Cu^{I} state was reached at the end of the TPR protocol. Comparing the two Cu-MOR compositions, the reaction led to the development of very similar spectral features in both samples, and it was therefore evident that more advanced analysis was necessary to search for composition-dependent differences in the spectra.

3.2 Finding spectroscopic fingerprints of different Cu-species with MCR-ALS analysis

By employing MCR-ALS analysis on the *in situ* XAS data, we obtained quantitative information on the Cu-speciation throughout the TPR experiments as this advanced data analysis technique provides detailed insight into the speciation and dynamics of the Cu species inside the zeolite.[19,68] The MCR-ALS analysis yielded a total of six principal components. The pure XANES spectra of the six components are reported in Fig. 2a, while their concentration profiles in the different experiments are reported in Fig. 2b. A pictorial representation of possible Cu-species linked with the pure XANES spectra discussed is finally provided in Fig. 2c. Firstly, focusing on the O_2 activation step of the protocol, two high-temperature (HT) Cu^{II} species, **Cu^{II}_HT_a** and **Cu^{II}_HT_b**, are recognized with very similar XANES signatures. The biggest difference is the shape and intensity of the WL, supporting a conserved coordination motif with only subtle differences in the first-shell bond distances and angles. It is plausible that they could stem from the same Cu-moiety, *e.g.*, a mono-μ-oxo dicopper(II) core, but docked at distinct zeolitic exchange sites, also featuring different accessibility. The third Cu^{II} species recognized, **Cu^{II}_LT**, is described as a low-temperature (LT) Cu^{II} species, since it increases in concentration with a decrease in temperature. **Cu^{II}_LT** is likely to be more highly coordinated than the high-temperature species, based on the higher WL intensity observed in this case. Interestingly, the growth of **Cu^{II}_LT** appears to correlate with a decrease in the concentration of **Cu^{II}_HT_a**, while

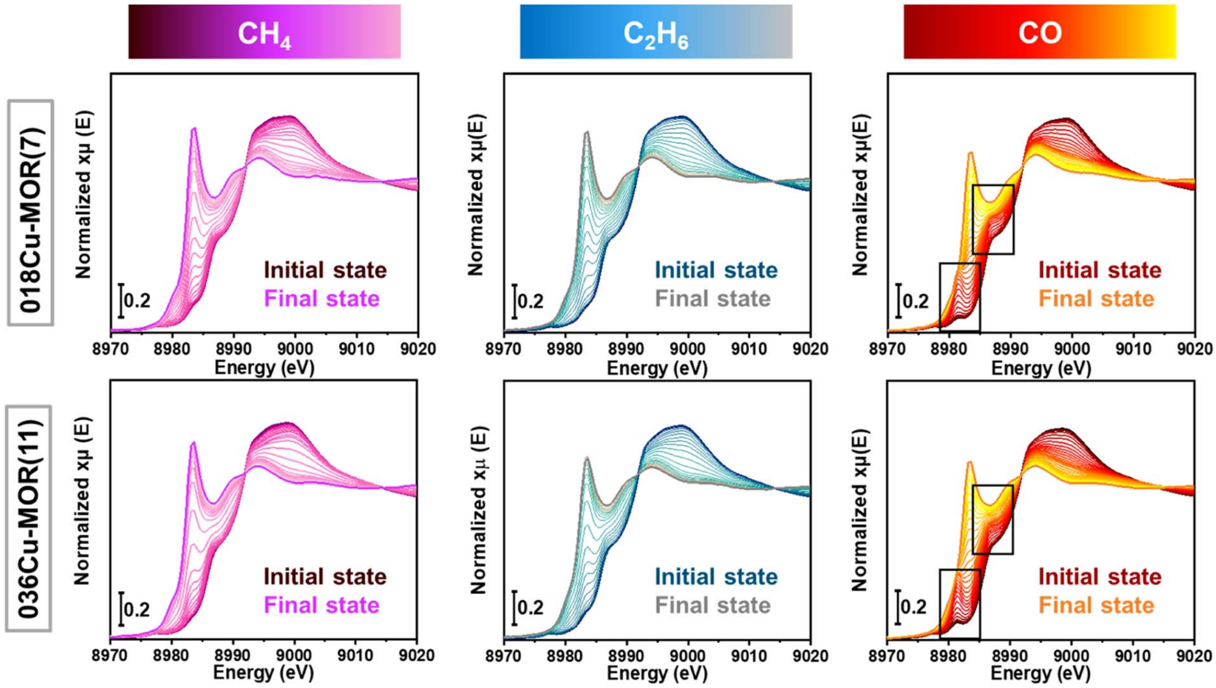

Fig. 1 XANES TPR spectra for each sample/reducing agent combination. The temperature was ramped up (5 °C min^{-1}) from 120 °C to 550 °C for 1.5 h. The increased intensity of the rising edge 1s → 4p peak related to Cu^{I} observed in all spectra, indicates the progressive formation of Cu^{I} species during the TPR experiments. A more complex situation is visible in the case of CO, in which an intermediate Cu^{I} species is detected (black boxes).

Cu^{II}_HT_b remains almost stable. We conjecture that the concentration of **Cu^{II}_LT** increases with decreasing temperature due to a dynamic change in some of the **Cu^{II}_HT_a** species, leading to a change in coordination motif from three-fold to four-fold. A minor peak in the typical Cu^{I} energy region (8983 eV) is visible in the pure **Cu^{II}_LT** XANES spectrum and is highlighted with an asterisk (*). This spurious spectral feature is an artifact from the MCR-ALS analysis due to a high abundance of Cu^{I} in the mix of Cu species, previously documented by Martini *et al.*[69]

When comparing the concentration profile for **Cu^{II}_HT_a** and **Cu^{II}_HT_b** between 018Cu-MOR(7) and 036Cu-MOR(11) during the O_2 activation, they behave similarly throughout all experiments, with a higher concentration of **Cu^{II}_HT_b** in 018Cu-MOR(7). Importantly, this is fully consistent with previous results by Pappas *et al.*, where a framework-coordinated Cu^{II} species with a Cu K-edge spectral signature consistent with **Cu^{II}_HT_b**, was found to be more abundant in the more productive 018Cu-MOR(7) sample, and tentatively associated with the active site for the MTM reaction.[18] Peculiarly, there is some discrepancy in the concentration profiles during the activation step for the CO-TPR experiment, where a higher concentration of **Cu^{II}_HT_a** is observed for both Cu-MOR zeolites. However, we allocate this error to uncertainties in the MCR reconstruction, possibly due to the high spectral similarity between **Cu^{II}_HT_a** and **Cu^{II}_HT_b**.

Upon shifting our focus to the TPR step of the protocol, it can be noted that new Cu-species develop, as Cu^{I} species form at the expense of Cu^{II}.[17] Depending on the experiment, three distinct principal components were detected, where **Cu^{I}_b** and **Cu^{I}_c** formed exclusively in C_2H_6 and CO, respectively. The two species denoted as **Cu^{I}_a** and **Cu^{I}_b** show similar spectral features, with a typical rising edge peak assigned to the 1s → 4p transition of Cu^{I}, and no trace of the d^{9} 1s → 3d pre-edge peak (Fig. 2a). The WL intensity is significantly lower than for the Cu^{II} species, indicating Cu sites with lower coordination number. Indeed, the spectral features are very similar to (quasi) linear Cu sites coordinated with two lattice O atoms.[70] The minor modifications in the XANES spectral shape between **Cu^{I}_a** and **Cu^{I}_b** are likely related to small induced differences in bond length and/or minor rearrangements when the sites are perturbed by the different gaseous species (CH_4 *vs.* C_2H_6). The XANES spectrum of the third Cu^{I} species, **Cu^{I}_c**, has very different spectral features from the other two, where the 1s → 4p peak is shifted towards lower energy values. This spectral fingerprint, clearly distinguishable in the experimental data, initially suggested the presence of an intermediate species during the CO-TPR ramp (Fig. 1). This implies that the coordination geometry and environment of this species is considerably different. When studying the concentration profile, Fig. 2b, we observe how the species reaches a maximum at about 260 °C and then slowly diminishes up until ∼400 °C. Due to the change in the coordination environment of this species compared to **Cu^{I}_a** and **Cu^{I}_b**, we conjecture the species is related to mono- or dicarbonyl complexes forming in the presence of CO, as CO is known to form stable adducts with Cu^{I} sites in zeolites.[39,40] A small fraction of **Cu^{I}_c** species is still detected above 400 °C for 036Cu-MOR(11), however, this quantity falls within the uncertainty

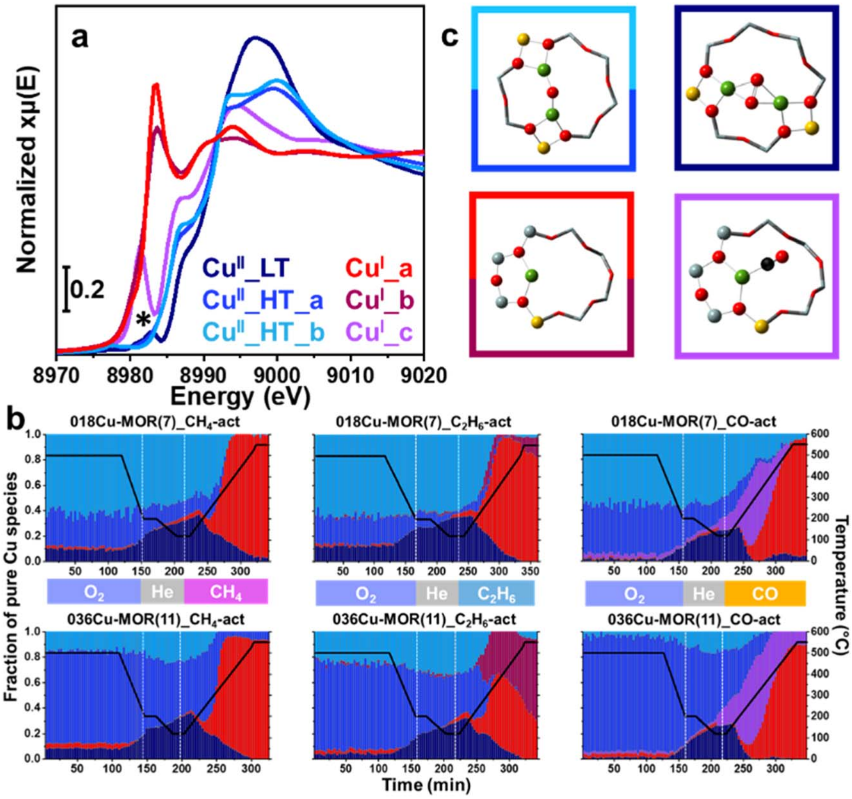

Fig. 2 (a) Global representation of the pure XANES spectra of Cu species obtained by MCR analysis, performed considering the whole dataset except for the ramp from RT to 500 °C during the activation step. The * symbol indicates an MCR reconstruction artifact. (b) Corresponding temperature-dependent concentration profiles for each Cu species, in which the evolution of the common species follow the same trends: **Cu^{II}_HT_b** is more abundant than **Cu^{II}_HT_a** in the 018Cu-MOR(7) sample, while the opposite is observed in 036Cu-MOR(11); **Cu^{I}_a** at the beginning of TPR forms preferentially from the **Cu^{II}_HT_b** species. In the CO case, the **Cu^{I}_c** intermediate species is visible in the first part of the TPR. (c) Pictorial representation of the Cu species proposed to form during the experiment. Atoms color code: Cu, green; O, red; C, black; Si, grey; Al, yellow.

typically associated with MCR-ALS reconstruction (∼10% of total Cu), and can therefore not be ascertained as a stable species.[69]

Lastly, it should be noted that when the Cu^{I} species start forming in the CH_4- and C_2H_6-TPR experiments, we see the consumption of **Cu^{II}_HT_b** slightly before the consumption of **Cu^{II}_HT_a**. This observation indicates that **Cu^{II}_HT_b** is more easily reduced upon alkane activation, and as this is the dominant Cu^{II} species in the most MTM active 018Cu-MOR(7) sample, we hypothesize the Cu reducibility to be linked with the activity of the samples. This hypothesis is considered even more closely in the following section, as we attempt to look more meticulously at the overall reduction trends during the TPR ramp.

3.3 Coupling Cu^{II} to Cu^{I} reduction with reactant consumption and product formation

To elucidate more easily the minor differences in the TPR protocol step between the two MOR compositions and the different substrates, the total Cu^{I} fraction during the TPR ramp is plotted in Fig. 3. The data points are derived by summing the fractions of all the pure Cu^{I} species as determined by the MCR-ALS analysis above for each XANES spectrum collected. The Cu^{I} fraction in 018Cu-MOR(7) and 036Cu-MOR(11) as a function of temperature during TPR is compared for all three reactants, CH_4, C_2H_6, and CO. In the bottom panel of Fig. 3, we report the first derivative of the trace (d(Cu^{I} tot.)/dE) to emphasize the reduction rate. Several interesting differences may be observed. Foremost, we observe that the onset of Cu reduction varies depending on the substrate in the order of $CO < C_2H_6 < CH_4$, where the CH_4 atmosphere leads to the highest reduction temperature. This is quite natural given the stronger bond dissociation energy of CH_4 (439 kJ mol^{-1}) compared to C_2H_6 (422 kJ mol^{-1}).[71] As the behavior of Cu in CO is markedly different, we will discuss further the CO-TPR event at the end of the section, and for now, focus on the results obtained with the two alkanes as reducing agents.

At first glance, the two Cu-MOR samples are behaving very similarly. Nevertheless, upon close examination, some small, but consistent differences can be observed. First, 036Cu-MOR(11) has a higher maximum reduction rate. This is specifically evident in the derivative plotted in the bottom panel of Fig. 3. Secondly, we observe that 018Cu-MOR(7) appears to have a marginal temperature region initially, where Cu is reduced faster than for 036Cu-MOR(11). This is consistent with

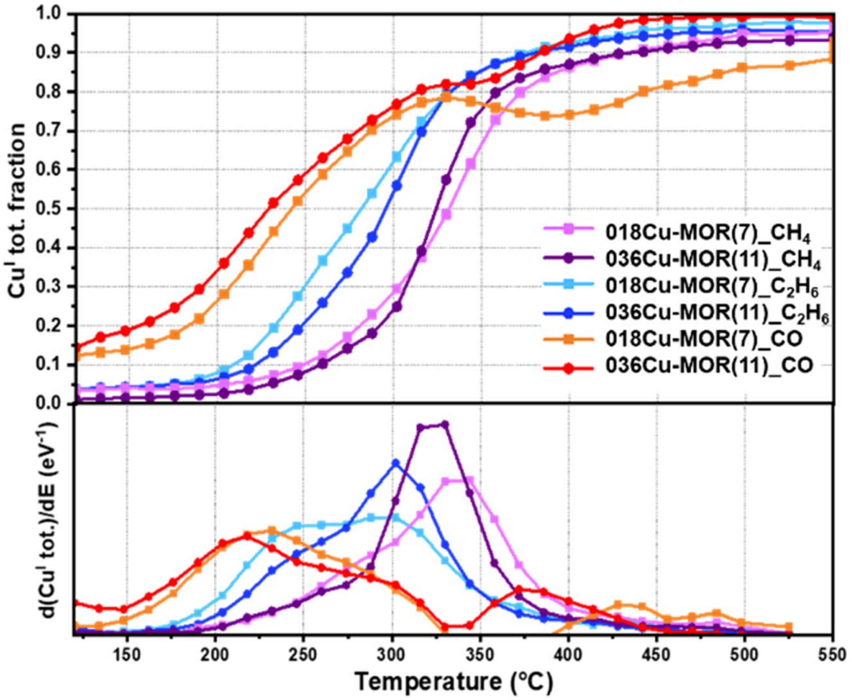

Fig. 3 Comparison of MCR-derived total Cu^I fraction as a function of temperature for each sample/reactant combination (top panel) in the CH_4-, C_2H_6-, and CO-TPR steps, and corresponding first derivative (bottom panel) to better identify inflection points in the Cu^I total fraction profile.

the **Cu^{II}_HT_b** species reducing faster than the other Cu^{II} species, as observed in the previous section. This earlier reduction behavior in 018Cu-MOR(7) could be sought-after evidence of more readily reducible species in the highly active Cu-MOR material.[18,33] A high "self-reduction" potential has been linked directly to the materials' methanol productivity in other framework topologies like Cu-exchanged FER and CHA.[12,14] This however, has not been observed for the Cu-MOR zeolites presented herein, as previously reported results have indicated that 018Cu-MOR(7) has more "self-reduction" resistant species, which then were coupled with well-distributed Cu-oxo species with high coordination and uniform bond lengths.[18,32] It should be noted, however, that the above-mentioned studies concern the reducibility of Cu-zeolites in either vacuum or inert atmosphere. Conversely, herein we are linking the high methanol productivity of 018Cu-MOR(7) directly to the reducibility of the Cu species in a methane atmosphere. This elucidates the importance of working with as relevant conditions as possible. Moreover, the higher reducibility observed for 018Cu-MOR(7) herein is in full agreement with Lomachenko *et al.* who found that more Cu^{II} reduced to Cu^I after methane loading for the 018Cu-MOR(7) material compared to 036Cu-MOR(11), when investigating the samples with XAS in a full MTM cycle.[23]

Upon comparing the reduction rate of Cu^{II} to the substrate consumption and CO_2 production obtained simultaneously from MS analysis of the reactor outlet (Fig. 4), interesting features are found. First, during CH_4-TPR, both CO_2, from overoxidation of CH_4, as well as the consumption of CH_4, appear in the same temperature window as the Cu^I formation. This direct link between CH_4 consumption, CO_2 production, and Cu^I formation contrasts with previously reported results by Sushkevich *et al.*[15] They observed a temperature region where CH_4 was consumed before CO_2 production over Cu-MOR (200 > 325 °C) and signified this window to be linked with oxidation processes of partially oxidized methane intermediates. However, as we observe the complete oxidation occurring simultaneously with Cu^I formation and CH_4 consumption, we speculate that with a continuous temperature ramp, the overoxidation occurs too fast to be singled out from the CH_4 consumption and Cu^{II} reduction in a meaningful way. Nevertheless, about 10% of the total Cu^I fraction is forming before the onset of CH_4 consumption (below 250 °C). We postulate this minor Cu^I fraction, yet very close to the uncertainty of the MCR-ALS method, to possibly come from a "self-reduction" of dimeric Cu^{II}-oxo sites to Cu^I, as made possible by an electron-rich environment after O_2 activation, where O^{2-} ions have remained stabilized in the framework.[72] We must point out that the results also show small traces of CO_2 produced in this low-temperature window. However, we allocate this to an effect of the low signal resolution caused by the small amounts of material and gas flows used in the experiment. Also due to this, we cannot exclude the possibility that some CH_4 (not visible in the CH_4 trace) is being consumed already from around 200 °C when Cu is being reduced. Regardless, some Cu^I is forming before consumption during C_2H_6-TPR, especially discernible for 018Cu-MOR(7), supporting the "self-reduction" event suggested above. Another intriguing observation during C_2H_6-TPR is that there is a secondary region, where no more ethane is being consumed, but there is still a reduction of Cu, as well as continued production of CO_2. This behavior indicates that

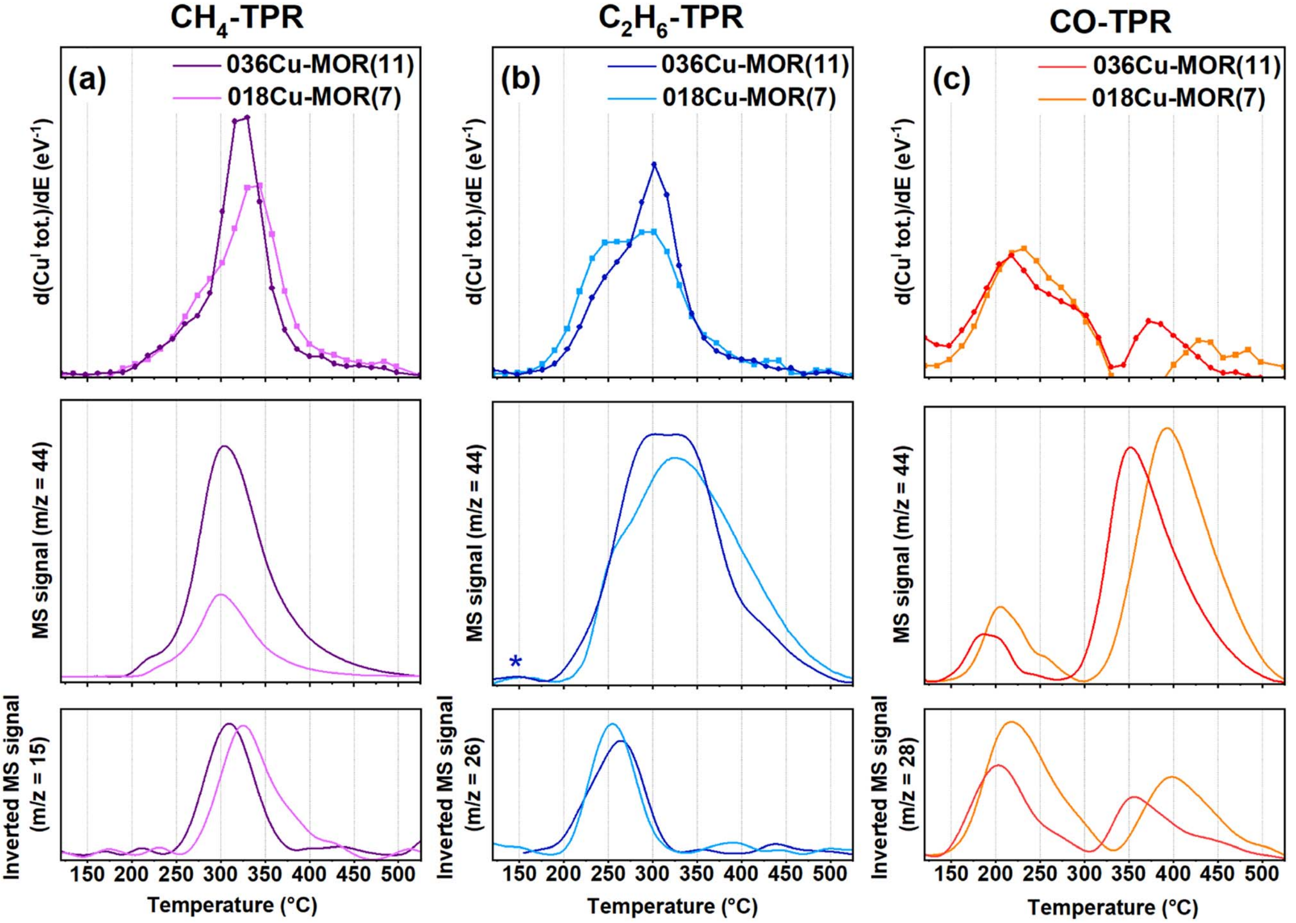

Fig. 4 (a–c) Comparison of the first derivative of the Cu^I fraction (top panel) to the CO_2 formation (middle panel) and reactant consumption (bottom panel) during the TPR protocol with (a) CH_4, (b) C_2H_6 and (c) CO. The MS trace used for CO_2 is $m/z = 44$, while $m/z = 15$, 26, and 28 is used for CH_4, -C_2H_6 and CO, respectively. The MS traces have been normalized to the sample weight and Cu content. *The CO_2 trace for 0.36Cu,H-MOR(11) during C_2H_6-TPR has been collected in a parallel experiment in the home laboratory, due to technical problems with the trace obtained during the XAS experiment.

when ethane acts as a substrate, there are secondary oxidation processes with fragments from ethane oxidation, that are less potent reducing agents, occurring on remaining Cu^{II} sites that did not react directly with ethane or were somehow not accessible to ethane.

Coming back to the CO-TPR protocol, two reduction regions are observed. The primary reduction starts directly upon contact with CO and leads to *ca.* 80% of reduced Cu^{II}. Then as the temperature increases, a secondary reduction event happens at higher temperatures, involving the residual fraction of *ca.* 20% of total Cu. For 018Cu-MOR(7), an apparent transient reoxidation involving <10% Cu^I can be observed at high temperatures. However, given the unlikely nature of this event, we assign this peculiar behavior to an error in the reconstruction of the XANES spectra. In contrast to the behavior of the Cu-zeolites in the alkane atmosphere, it appears the Cu-sites in 036Cu-MOR(11) reduce in a lower temperature range. Focusing on Fig. 4, we surmise that the first, broad reduction peak is linked with the above-suggested formation of Cu^I–$(CO)_x$ ($x = 1$ or 2). This is also well supported by a clear consumption of CO, and a smaller CO_2 production coming from the oxidation at the Cu-oxo sites. Then, during the high-temperature reduction event, we do see a much larger fraction of CO_2 being produced in combination with a smaller consumption of CO. As most Cu already has been reduced to Cu^I at this point, we postulate that the production of CO_2 is linked with trapped CO_2 being released as the temperature increases, or possibly the release and oxidation of CO from Cu^I–carbonyls. This could proceed *via* a reaction with residual O^{2-} present, or by a disproportionation reaction between two CO molecules in a Boudouard reaction.[73] As we do not have any evidence for the formation of elemental C, the latter reaction pathway is only speculations by the authors at this point.

3.4 Complementary *in situ* UV-vis TPR experiments

To support the observations presented in the previous sections, a complementary experiment was performed in-house with a purpose-designed *in situ* UV-vis setup. The UV-vis spectra were obtained in diffuse reflectance mode during a CH_4-TPR experiment for both 018Cu-MOR(7) and 036Cu-MOR(11) and are

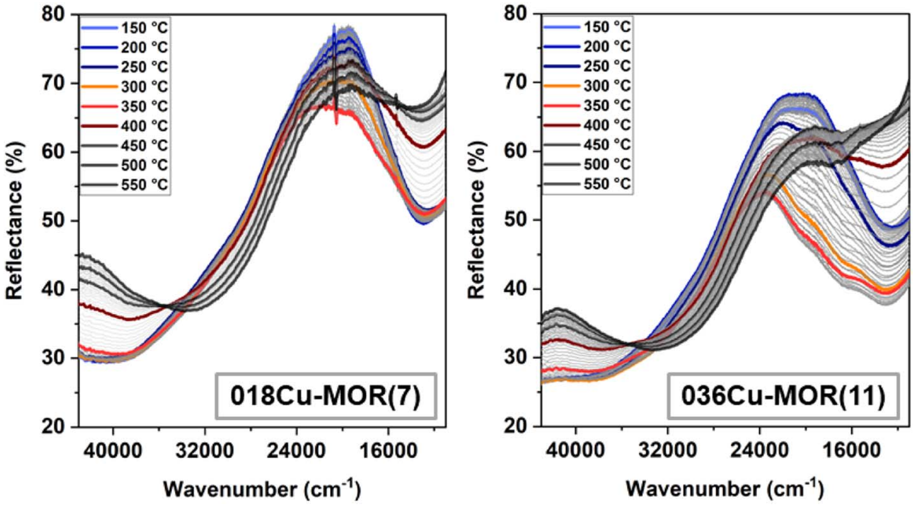

Fig. 5 *In situ* UV-vis spectra were obtained during a TPR protocol with CH_4 for the two Cu-MOR samples. The spectra are overlayed, with a thick line, and different colors are used for every 50 °C to clarify the change in the spectra throughout the protocol. Blue colors are for low temperatures, red for intermediate temperatures, and dark grey for high temperatures.

reported in Fig. 5. Even though we here operated with a different sample amount and gas flow, the CH_4 consumption and CO_2 production followed closely the same temperature window (~250–400 °C) as obtained during the *in situ* XAS experiments. The MS traces for CH_4 and CO_2 are reported in the ESI, Section S6.† Interestingly, we are also seeing the biggest changes in the UV-vis spectra in the same temperature window. We observe that at about 250 °C, three bands at 20 250, 16 850, and 13 000 cm^{-1} grow, reaching a maximum at about 325 °C. This is also approximately the temperature at which a maximum is observed for CH_4 consumption and Cu^I formation rate during the XAS experiment. At 325 °C, the bands decrease again, giving the biggest evidence of reduction from Cu^{II} to Cu^I, as this is what one would expect when the Cu ion goes from a d^9 configuration to a d^{10} configuration, where the d–d electron transfer is forbidden. When the temperature reaches about 400 °C, the changes slow down, and mostly temperature-induced shifts in the ligand to metal charge transfer (LMCT) region (25 000–45000 cm^{-1}) are observed from 450–550 °C.[74] The final state reached at 550 °C shows for both samples a rather flat profile in the d–d spectral range, consistent with the virtually pure Cu^I state revealed by XAS. The weak negative features still observed at the end of the TPR around 16 000 cm^{-1} most likely stem from a combination of high-temperature background fluctuations and, possibly, residual traces of highly absorbing Cu^{II} species (*vide infra*), with abundance below the XAS detection limit.

The growth of the bands in the d–d region between 250 and 325 °C, especially visible in 036Cu-MOR(11), is counter-intuitive, as it could be at first glance interpreted as an increase in the abundance of Cu^{II} species. However, the combination of these three bands shares similarities with the so-called "multiplet" formation also observed previously in Cu-CHA during O_2 activation.[75] The literature suggests that the multiplet formation is linked with a diluted Cu^{II} species with a very strong extinction coefficient.[76] Interestingly, it is evident from the band at 38 500 cm^{-1} that the species must also affect the LMCT region, as there is no evidence of reduction here before the temperature reaches 325 °C. Nevertheless, we conjecture that even though this species is forming, it is likely to involve a minor fraction of total Cu ions, and there is still a reduction process occurring before $T = 325$ °C, as evidenced by the XAS experiments. To the best of our knowledge, the observation of a multiplet has not previously been reported for Cu-MOR. The Cu^{II} species is temperature dependent, and forms, contrary to Cu-CHA, in a CH_4 atmosphere. Why this species is much more prominent in 036Cu-MOR(11) than in 018Cu-MOR(7) would only be subject to speculation at this point, but it is alluring to suggest it is linked with the **Cu^{II}_HT_b**, as this is much more abundant in the 036Cu-MOR(11) sample.

3.5 MCR-ALS-derived EXAFS spectra

By analyzing the EXAFS region, we get further information on the local environment of Cu ions after key steps in the TPR protocols (Scheme 1). Since the results thus far have shown the same Cu species in 018Cu-MOR(7) and 036Cu-MOR(11), we decided to combine data obtained over both zeolites to optimize the signal quality in the EXAFS region. As we had performed an MCR reconstruction on the whole data set, including the EXAFS energy range, the EXAFS spectra could be obtained directly from the MCR-derived $\mu(E)$ spectra by following a recently reported approach.[45] This allowed us to get EXAFS signals of the pure Cu species dominating Cu-speciation in the key experimental steps. The EXAFS signals were then extracted with standard procedures and visualized in both *k*- and *R*-space (Fig. 6). To guarantee signal reproducibility while avoiding as much as possible high-*k* noise, the Fourier Transform was performed in a narrow *k*-range from 2.5–9.0 Å^{-1} (grey box in Fig. 6a), see ESI, Section S5† for more details. The collection temperature is

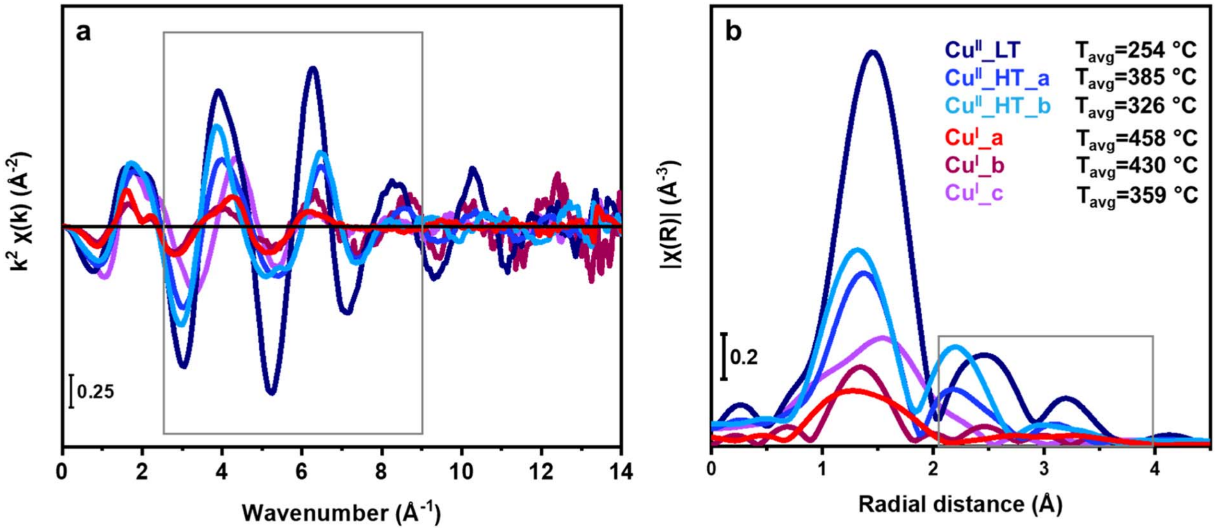

Fig. 6 (a) MCR-ALS derived k-space EXAFS spectra for the pure Cu species identified. The k range used to calculate the FT, 2.5–9.0 Å^{-1}, is highlighted by the grey box. (b) Corresponding FT-EXAFS spectra in R-space, obtained by Fourier transforming the $k^2\chi(k)$ curves reported in (a). According to the structure of the zeolite, the peaks highlighted by the grey box could be related to Al, Si. and the farthest O atoms from the MOR lattice or to other extra framework copper atoms participating in multimeric Cu species.

known to strongly influence the EXAFS oscillation intensity, being increasingly dampened as temperature increases.[77] This is due to an effect of the Debye–Waller factor in the EXAFS equation. As the MCR-ALS derived EXAFS spectra are obtained from the collective analysis of a temperature-dependent dataset, we have defined an average temperature associated with each spectrum to guide the interpretation of the EXAFS spectra. In particular, for each i^{th} pure species, a reference average temperature, T_{avg}i, representing the weighted average temperature using the MCR-derived concentration of each scan in the dataset as weights, was calculated (ESI, Section S4†). The temperature dependence is evident in the $k^2\chi(k)$ spectra reported in Fig. 6a. All HT Cu$^{\text{II}}$ (**Cu$^{\text{II}}$_HT_a** and **Cu$^{\text{II}}$_HT_b**) species show dampened oscillations compared to **Cu$^{\text{II}}$_LT**. This is consistent with the latter having a significantly lower T_{avg}i value (254 °C *vs.* 385 and 326 °C, respectively for the HT Cu$^{\text{II}}$ species). Then, compared to the Cu$^{\text{II}}$ species, the $k^2\chi(k)$ curves of all Cu$^{\text{I}}$ species present lower signal amplitudes and detectable frequency differences, regardless of temperature. Hence, we point out that the oxidation state of the absorbing atom, although not directly monitored by EXAFS, is relevant for further discussion, as it influences the average number and distribution of atomic neighbors and, to some extent, their interatomic distance from the Cu centers. Finally, we note that the EXAFS spectra in k-space of **Cu$^{\text{I}}$_a** and **Cu$^{\text{I}}$_b**, as well as **Cu$^{\text{II}}$_HT_a** and **Cu$^{\text{II}}$_HT_b**, are very similar, again pointing to the structural similarities between these species as suggested above.

By analyzing the FT-EXAFS spectra shown in Fig. 6b, we can get more information on the Cu environment of the different pure components. The first-shell peak corresponds to single-scattering (SS) contributions involving framework (O_f) and extra-framework oxygen (O_{ef}) atoms.[78] A higher intensity in the first shell should be linked with higher Cu coordination and a lower T_{avg}i temperature, which fit well with the proposed Cu$^{\text{I}}$ and Cu$^{\text{II}}$ speciation, based on the MCR-ALS derived pure XANES spectra (Fig. 3b). In addition to **Cu$^{\text{I}}$_c** having a higher first-shell peak than the other Cu$^{\text{I}}$ species (indicating higher coordination), the structured shape of the first-shell peak suggests the presence of another scattering contribution in addition to O_f and O_{ef}. The observed shift of the first shell maximum to higher R is also consistent with an earlier study of CO interacting with Cu$^{\text{I}}$-ZSM-5.[79] Combined with the XANES results indicating a Cu$^{\text{I}}$–CO formation, we accredit this contribution to the carbon atom in a CO ligand.

A well-defined second shell peak is visible in the Cu$^{\text{II}}$ species. This we attribute, based on previous studies, to a framework bound Al near the Cu atoms (*ca.* 2.8 Å).[80] Importantly, the presence of this signal for the **Cu$^{\text{II}}$_LT** FT-EXAFS eliminates the possibility of **Cu$^{\text{II}}$_LT** being a mobilized, hydrated Cu$^{\text{II}}$ species, as hydration of Cu would dampen this signal. In **Cu$^{\text{I}}$_a** and **Cu$^{\text{I}}$_b**, the second-shell region is strongly dampened. This is consistent with previous studies on "self-reduced" Cu-MOR, causing a higher degree of structural disorder in the Cu$^{\text{I}}$ cation local environment, which ultimately led to destructive interference between the EXAFS scattering paths.[34,70,80]

The third shell peak (3.0–3.3 Å), although, only visible for Cu$^{\text{II}}$ species, could stem from several types of scattering contributions with similar radial distances like framework Si/Al/O atoms or Cu atoms in multimeric moieties. To unravel the contributions in the third shell, we performed Wavelet Transform (WT) analysis on the EXAFS data.

3.6 Shedding light on the nuclearity of Cu-species with WT-EXAFS analysis

The limitations of conventional, FT-EXAFS analysis in the assignment of the third shell EXAFS contributions can be solved by performing a WT-EXAFS analysis, where information on interatomic distances from the *R*-space is combined with element-specific information obtained from *k*-space.[57–59] In *k*-space, Cu–Cu scattering paths can be discriminated from those involving framework Si/Al/O atoms due to a different EXAFS backscattering amplitude function ($F(k)$) of the elements, leading to a *k*-value that is element-specific. The typical Cu–Cu distances of dicopper(II)-oxo species in zeolites is ~3.5 Å.[34,80] An example of the resulting WT-EXAFS density maps is depicted in Fig. 7. We remind that this and all the WT-EXAFS maps reported herein are obtained by applying a Morlet Wavelet Transform (see Section 2.5) to the MCR-derived $k^2\chi(k)$ pure EXAFS spectra reported in Fig. 6a. In part (a), the full-range WT-EXAFS map for a representative pure Cu species, **Cu^{II}_HT_a**, is given. The first lobe located at Δk (0–12.5) Å^{-1} × ΔR (0.5–2.0) Å is from O_f and O_{ef} first shell SS contributions. The elongation effect of this low-*R* first lobe towards higher *k*-values is due to spectral broadening, well explained by Timoshenko *et al.*[59] The more interesting high-*R* EXAFS contributions are magnified in Fig. 7b for better visualization. The $F(k)$ functions for the relevant atoms (O, Al, Si, and Cu) are presented above in Fig. 7b to aid in the sub-lobe assignment. Two sub-lobes are detected. The low-*k* sub-lobe (~3 Å^{-1}) indicates the contributions of lighter elements (O, Al, and Si), while the second, high-*k* sub-lobe at ~7 Å^{-1}, fit well with the maximum of the Cu backscattering function and can undoubtedly be assigned to Cu–Cu scattering contributions.[60,61]

To compare the WT-EXAFS maps of the six pure Cu species more easily, the maps were integrated in the relevant *R*-space range, giving the power density functions of the Cu species. The power density functions are reported in Fig. 8, together with the WT-EXAFS maps of the high-*R* EXAFS region for all Cu species. In both representations, the position of the sub-lobes provides valuable information on the elemental identity of the atomic neighbors surrounding the Cu absorber in the radial distance of interest. When comparing the power density functions of the Cu^{II} species, they all have detectable Cu–Cu contributions, visible from the high-*k* sub-lobe, in the accessible *R*-space range, leading us to describe these species as dicopper(II) moieties (or proximal Cu^{II} monomers), also in line with previous literature proposals.[3,18,60,61] Consistently with previous studies on the use of CO dry oxidation to titrate dicopper(II) species in zeolites,[42,43] having most of the Cu organized into dimeric species at the end of the oxidative pre-treatment falls in line with the effective reduction observed during CO-TPR, already in the 150–300 °C range.

We observe that the signal intensity of the Cu^{II} species decreases with increasing temperature (T_{avg}i) in the whole *k*-range, which is consistent with the temperature dependence of EXAFS spectra and cannot be directly linked with a reduction in the coordination number of specific species. However, the two sub-lobes distinctly have the same intensity in **Cu^{II}_LT** which is not the case for the HT Cu^{II} species, where the high-*k* sub-lobe has a lower intensity. Dealing with pure-species WT-EXAFS, this observation can solely be linked to differences in the Cu–Cu

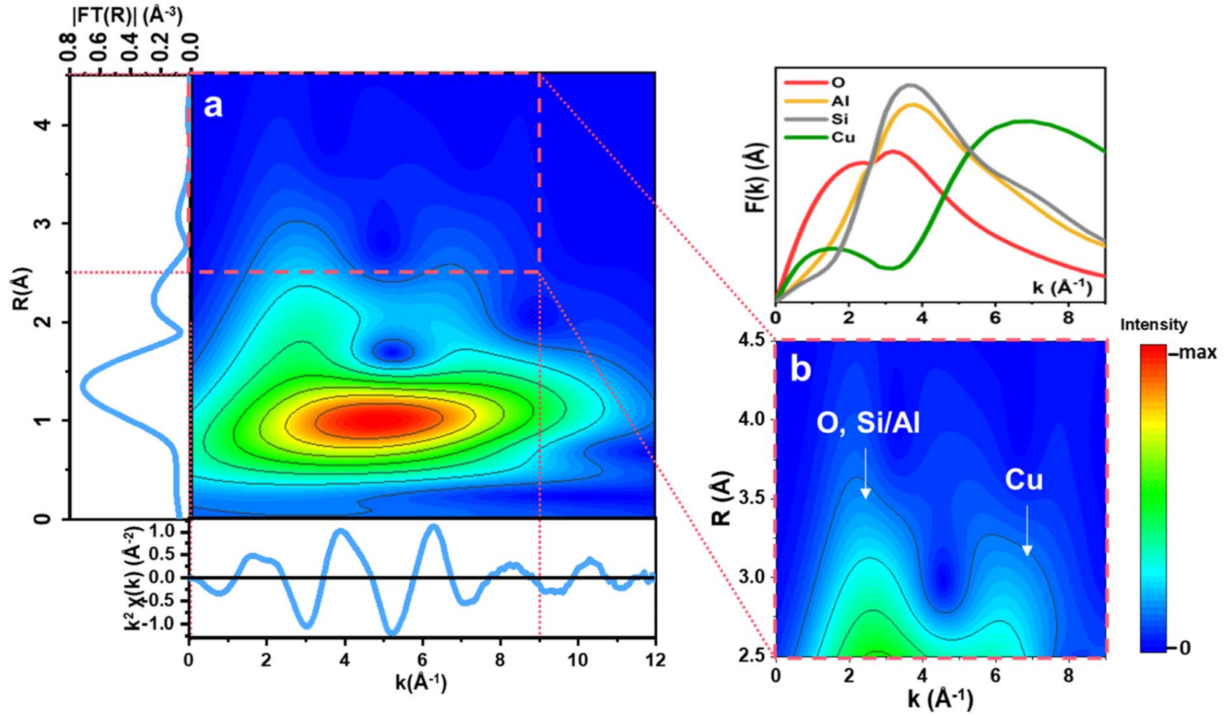

Fig. 7 (a) Full-range WT representation of the EXAFS signal for a representative pure Cu species, namely Cu^{II}_HT_a, formed at high temperature during the pre-treatment step. (b) Magnification of the high-*R* WT region highlighted by the red dashed box in (a), in the ranges Δk (0–9) Å^{-1} and ΔR (2.5–4.5) Å. On the top is reported a plot of the relevant backscattering amplitude functions, $F(k)$, calculated from FEFF6.0 considering SS paths involving O, Si, Al, and Cu scatterers.[34]

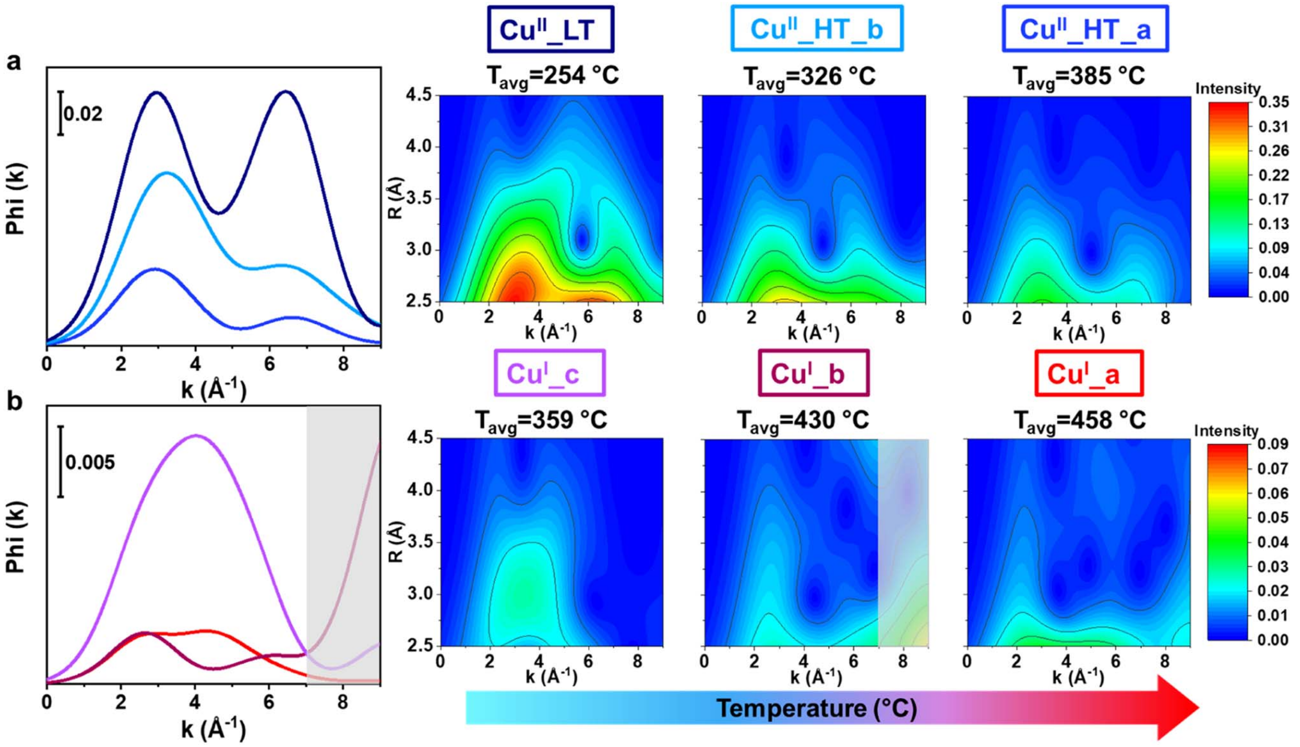

Fig. 8 (a and b) Power density functions (left) and WT maps (right) obtained by WT-EXAFS analysis for (a) Cu^{II} species and (b) Cu^{I} species. For each i^{th} species, the average temperature (T_{avg}i) is reported. The shadowed grey boxes in (b) highlight the high-*k* range affected by possible artifacts due to poor S/N ratio in the MCR-derived $k^2\chi(k)$ curves for **Cu^{I}_b**.

interatomic distance. Indeed, considering the inherent dampening of the EXAFS contributions as the interatomic distance increases, the observed differences in the relative intensities of the low- and high-*k* peaks point to a longer Cu–Cu distance in the two HT Cu^{II} species compared to **Cu^{II}_LT**. Looking at Fig. 8, is possible to identify differences in the signal distribution of the second sub-lobe in Cu_HT species, suggesting a shorter Cu–Cu interatomic distance in **Cu^{II}_HT_b** with respect to **Cu^{II}_HT_a**. Indeed, the former species shows a distinctly higher intensity in the 2.5–3.0 Å *R*-space range, consistent with the slight shift towards lower *R*-values visible by comparing the FT-EXAFS spectra of the two species in Fig. 6b.

Focusing on the Cu^{I} species (Fig. 8b), the low-*k* WT-EXAFS signals associated with **Cu^{I}_a** and **Cu^{I}_b** are overall weaker and broader concerning what is observed for the Cu^{II} species. This is consistent with the FT-EXAFS results and is due to the already-mentioned structural disorder in the second-shell region and the relatively high temperature at which the Cu^{I} species form. Conversely, the power density function and WT-EXAFS map of **Cu^{I}_c** present a dominating peak/sub-lobe shifted towards higher *k* values ($k = 4$ Å^{-1}) compared to the sub-lobe detected in the WT-EXAFS map of the Cu^{II} species ($k = 3$ Å^{-1}). Based on the above-mentioned observations, we assign this sub-lobe to the presence of additional single and multiple scattering contributions from Cu–C/O in Cu^{I}–carbonyl adducts, reinforcing the assignment of **Cu^{I}_c** to Cu^{I}–$(CO)_x$ complexes (*vide infra*). Focusing on the high-*k* region for the Cu^{I} species, it is impossible to detect a well-defined sub-lobe at *ca.* 7 Å^{-1}, as it was for the Cu^{II} moieties. We note an intensity increase above *ca.* 8 Å^{-1} for the **Cu^{I}_b** species (shadowed grey boxes in Fig. 8). However, due to poorer S/N ratio in the MCR-derived $k^2\chi(k)$ curve for this species, likely also due to the high $T_{avg}^{Cu(I)\_b}$ (430 °C), we allocate the intensity increase to an artifact that causes a spurious signal increase in the high-*k* portion of the WT map that cannot be safely interpreted. Accordingly, we recognize that the absence of a high-*k* sub-lobe in the Cu^{I} species corroborates previous studies suggesting that multimeric copper-oxo moieties are cleaved during reduction, forming isolated Cu^{I} ions that have Cu–Cu interatomic distances higher than the EXAFS-accessible *R*-space range.[80]

3.7 Confirming the formation of Cu^{I}–CO with *in situ* FT-IR spectroscopy measurements

To verify that the **Cu^{I}_c** component is indeed from Cu^{I}–$(CO)_x$ formation, and whether it is linked with mono- or dicarbonyl species, we performed *in situ* CO-TPR experiments coupled with FT-IR spectroscopy on a pre-oxidized 018Cu-MOR(7) sample. The results are reported in Fig. 9a. As CO atmosphere is introduced to the sample, a band at 2158 cm^{-1} evolves slowly, confirming the formation of some Cu^{I} species that is then available to form Cu^{I}–CO adducts on Cu-MOR zeolites.[81] Additionally, we observe the presence of the gaseous phase of CO, contributing with the presence of rotational-vibrational branches on both sides of the Cu^{I}–CO band. The maximum intensity of these branches is marked with an asterisk (*). Then, as the

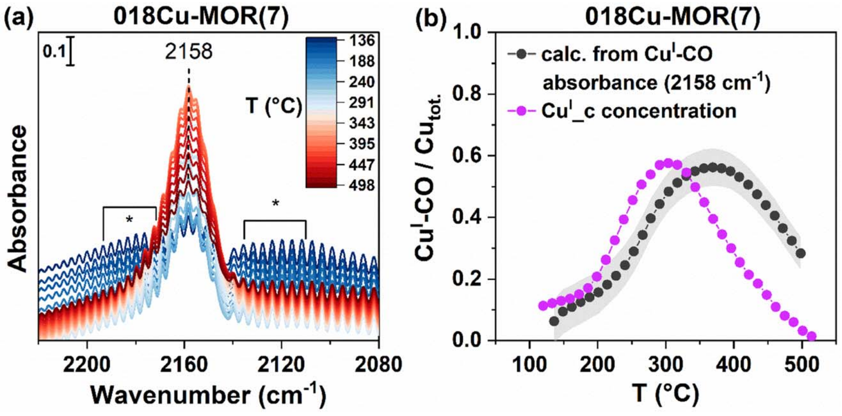

Fig. 9 (a) FT-IR spectra obtained during CO-TPR. Spectra are background subtracted. (b) A comparison of the fraction of Cu^I–CO species found with XAS throughout the TPR protocol (**Cu^I_c**), and the corresponding Cu^I–monocarbonyl fraction calculated from Lambert–Beer law by integrating the band at 2158 cm^{-1}. The error bars (grey band) are given as the standard deviation determined from three different baseline positions on the rotational–vibrational features when obtaining the integrated area.

temperature increases, the monocarbonyl band increases, until a maximum is reached at about 350 °C. The intensity of the band at 2158 cm^{-1} reflects both the amount of Cu^I (growing according to the reducing effect of CO) and the stability of the Cu^I–CO adducts. For this reason, it is not directly coinciding with the evolution of the **Cu^I_c** component, which is found to have a maximum at about 300 °C (Fig. 2b), however, clearly present up to at least 400 °C. The formation of a Cu^I–CO band on a Cu zeolite with no Cu^I as evidenced by XAS, suggests that at 120 °C, CO is instantaneously able to reduce some Cu^{II} species to Cu^I, that are then able to form the Cu^I–CO adduct and form CO_2. This is consistent with the reduction of Cu^{II}, the early consumption of CO, and the subsequent formation of CO_2, as observed above when performing the parallel CO-TPR/XAS experiment. Due to the strong presence of rotational-vibrational features, CO-TPD was also performed to verify that only monocarbonyl species form when exposed to CO and that the prolonged presence of the 2158 cm^{-1} band was indeed due to a strong interaction with the framework-coordinated Cu^I ions, and not due to the presence of gaseous CO. The results are reported in ESI, Section S7,† and show undoubtedly the Cu^I–CO band at 2158 cm^{-1}, with no presence of the symmetric or asymmetric stretches of dicarbonyl species.[81] The band decreases in intensity with temperature but is not completely lost until $T = 300$ °C. This suggests that even without a constant atmosphere of CO, the monocarbonyl has a strong interaction with the Cu sites, confirming that Cu^I–CO is the intermediate species observed during CO-TPR.

To more quantitatively compare the temperature-dependent evolution of the 2158 cm^{-1} band from FT-IR with the evolution of the **Cu^I_c** component, we calculated the CO concentration from the integrated feature at 2158 cm^{-1} by applying the Lambert–Beer law given in eqn (3). Deplano *et al.* recently determined the molar attenuation coefficient, ε, for monocarbonyl species forming on Cu-ZSM-5 zeolites,[40] and as long as the band shape of the Cu^I–CO band is similar, this value should be somewhat comparable for other zeolite systems. We therefore used this value for our calculations herein. By dividing the calculated CO concentration by the total Cu concentration of the system we indirectly find the fraction of Cu^I–CO species with FT-IR. The results are reported in Fig. 9b, and lead to a strong correspondence with the **Cu^I_c** concentration determined by XAS. Both traces give a maximum Cu^I–CO formation (~300 °C) of about 55% of the total Cu concentration in 018Cu-MOR(7). At this temperature, almost 80% of the Cu in the sample has become Cu^I (Fig. 3), indicating that some CO species have already desorbed, leaving bare Cu^I sites. The CO reduction on Cu^{II} sites is a two-electron process, and should therefore only be possible on Cu-dimers, or possibly two isolated Cu^{II} species nearby.[44] Overall, these results, combined with the WT-EXAFS results described above, suggest that a very large fraction of the Cu-species are forming dimeric species already after O_2 activation, and do not need to be made mobile with, *e.g.*, an NH_3 molecule to form the dimers, as suggested for other zeolite systems, like CHA.[43,82] We note that there is a small shift in the temperature profile for the CO/Cu trace (calculated from absorbance) compared to **Cu^I_c**; nonetheless, we allocate this to the different setups utilized, causing small variations in the measured temperature. Additionally, we explain the slower CO desorption in the FT-IR setup to the vast difference in the sample environment. FT-IR was measured on a thin wafer, while XAS was performed on a pelletized sample in a capillary reactor. The different pellet morphology and sample environment likely leads to a slower diffusion through the sample in the FT-IR cell compared to the capillary.

4 Discussion

In the previous sections we have combined advanced spectroscopy methods in different spectral ranges with qualitative MS analysis to accurately determine the chemical nature, local structure and abundance of Cu species formed in two representative Cu-MOR samples after pretreatment in O_2 and subsequent TPR using CH_4, C_2H_6 and CO as reducing agents/

substrates. The two studied Cu-MOR samples were selected based on their significantly different performance in the direct MTM conversion,[18,23] and the results obtained herein unlocked novel insights on the Cu active site for this iconic reaction.

In this section, we critically discuss the obtained results in view of previous literature findings, to underline how the innovative approaches implemented in this work could contribute to deepen the atomic-scale understanding of Cu-zeolite based materials towards selective C–H bond activation. To this aim, Scheme 2 summarizes the main Cu-species identified throughout our experiments, illustrating their dependency on temperature, gas feed and compositional characteristics of the samples. We will examine separately the two key steps addressed in this work, namely the Cu^{II} speciation after pretreatment in O_2 and reduction dynamics/Cu^{I} speciation under TPR conditions.

4.1 Cu^{II} speciation after pre-treatment in O_2

Resolving the Cu speciation in zeolites after high-temperature thermal treatment in O_2 represents an essential, yet challenging, step before further analysis of Cu reactivity/reducibility is undertaken. A number of possible species has been proposed in literature, depending on zeolite topology, compositional characteristics, and synthesis/pre-treatment conditions.[19,30,83] The experimental findings obtained here, including for the first time MCR-ALS-based extraction of pure EXAFS spectra and their visual interpretation by WT, points to mono-μ-oxo dicopper(II) cores as dominant configurations at 500 °C in O_2. Consistently with previous HERFD-XANES analysis of the same samples,[18] two closely related components are found at 500 °C, namely **Cu^{II}_HT_a** and **Cu^{II}_HT_b**, with sample-dependent relative abundance (see pie charts in Scheme 2a) and shorter Cu–Cu interatomic distance in the latter component. According to recent literature,[63,64,84] different Cu–O–Cu angles (and thus Cu–Cu internuclear separation) in mono-μ-oxo dicopper species can influence the selectivity and reactivity of dicopper sites for MTM. In particular, according to Artsiusheuski *et al.*,[84] dicopper cores featuring a smaller Cu–O–Cu angle and a shorter Cu–Cu distance are characterized by a higher selectivity towards methanol and promoted at low Cu loading. This is fully consistent with both the MCR-ALS analysis and testing results reported previously for 018Cu-MOR(7) and novel structural insights obtained here, where WT-EXAFS indicate a shorter Cu–Cu distance in **Cu^{II}_HT_b**, which is the more abundant species in 018Cu-MOR(7). In parallel, the clear Cu–Cu scattering signal in WT-EXAFS for both HT Cu^{II} species, allows ruling out *trans*-μ-1,2-peroxo-dicopper(II) species, which would imply an excessively long internuclear separation (typically > 4 Å (ref. 85)), not consistent with the observed signal. In contrast, "coupled" $[CuOH]^+$ monomers remain a plausible alternative for **Cu^{II}_HT_a**. The coupled monomers, also recently considered among the viable MTM active sites,[86] would conserve the same tridentate coordination motif as mono-μ-oxo dicopper and, assuming Cu–Cu distances up to *ca.* 3.3 Å range, would fit with the Cu–Cu scattering observed in WT-EXAFS.

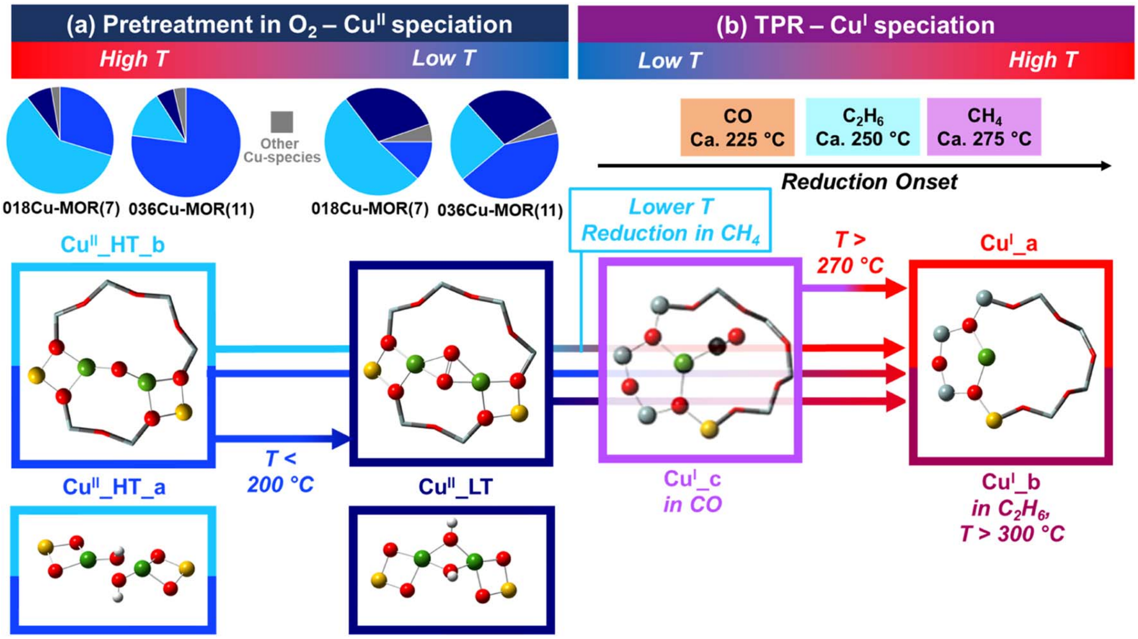

Scheme 2 Summary of the identified Cu species and their evolution as a function of temperature, gas feed and Cu-MOR composition. (a) Cu^{II} speciation after pre-treatment in O_2; pie charts illustrate the fractions of Cu-species determined by XANES MCR analysis at 500 °C in O_2 and at 120 °C in He just before exposing to the selected reducing agent (Fig. 2b, averaged values over all the available datasets). (b) Reduction behavior and Cu^{I} speciation under TPR conditions with CH_4, C_2H_6 and CO; reduction onsets are estimated based on the temperature values corresponding to the first maximum in the first derivative curve of the Cu^{I} tot. (*T*) profiles (Fig. 3, bottom panel). In all cases, pictorial models of the identified Cu species are reported; in part (a) the main assignments are displayed in the top boxes, while plausible alternatives, also consistent with our spectroscopic findings, are shown in the bottom boxes. Atoms color code: Cu, green; H, white; O, red; C, black; Si, grey; Al, yellow.

Importantly, we observe changes in Cu^{II} speciation while cooling down from 500 to 120 °C, under O_2/He flow, mostly connected with an increase in the concentration of **Cu^{II}_LT**, preferentially forming at the expense of **Cu^{II}_HT_a**. A similar behavior was already reported for both Cu-CHA and Cu-MOR zeolites,[46] but was not quantitatively addressed by MCR analysis. Both the XANES and the EXAFS features of **Cu^{II}_LT** points to a four-fold coordinated, multimeric Cu^{II} species. The species increase in abundance also when the feed is switched from O_2 to He in the final cooling step before TPR. A plausible assignment starting from a mono-μ-oxo dicopper(II) core could entail bis-μ-hydroxo dicopper(II) formed upon interaction with residual H_2O traces, favored as temperature decreases. This hydroxo-bridged dicopper(II) species is specifically discussed in enzymatic systems and complex formation,[87,88] but a similar hydration event forming trimeric Cu species in zeolites has also been suggested.[89] In a recent theoretical study on Cu-CHA,[90] Göltl *et al.* indicated such hydroxylated dicopper(II) species as the most stable around the typical CH_4 exposure conditions, and plausibly active towards MTM. Alternatively, μ-η^2,η^2-peroxo-dicopper(II) species could be proposed as a way for the system to prevent self-reduction by using O_2 molecules supplied in the first part of the cooling step. A resonance structure between the latter species and a bis-(μ-oxo) dicopper cluster has been recently proposed to describe MTM-active cores in Cu-FER.[91]

4.2 Reactivity and Cu^{I} speciation under TPR conditions

MCR-ALS analysis of XAS data obtained under consistent TPR conditions revealed a common linear **Cu^{I}_a** species for all the three reducing agents employed. Its spectroscopic signature is fully consistent with bare Cu^{I} ions coordinated to the MOR framework.[34,70] Overall, the XAS results obtained under CH_4-TPR well align with the recent report by Artsiusheuski *et al.*,[92] confirming for Cu-MOR the absence of either metallic or oxidic aggregates at the end of the TPR step. Nonetheless, during both C_2H_6- and CO-TPR, additional Cu^{I} species were found. **Cu^{I}_b**, observed at $T > 300$ °C during C_2H_6-TPR is again a quasi-linear Cu^{I}, likely with a slightly different geometry/siting with respect to **Cu^{I}_a.** Considering the recent findings about ethane-to-ethylene conversion over Cu-MOR,[93] both the reactant and the formed hydrocarbons could trigger long-range interactions leading to certain distortion in the Cu^{I} centers local coordination, especially in the high-temperature portion of the TPR. The **Cu^{I}_c** species found during CO-TPR was established herein as a chemisorbed Cu^{I}–CO intermediate by the combination of results from XAS and FT-IR. We were also able to verify the number of Cu^{I}–CO species formed throughout the TPR protocol by quantifying the absorbance observed with FT-IR. By exploiting CO oxidation as a probe reaction to titrate dimeric Cu species in zeolites,[42,43] CO-TPR results also showed, in agreement with WT-EXAFS, that dicopper(II) species are largely dominant in both Cu-MOR samples before reductant exposure.

By coupling the transformation of Cu^{II} to Cu^{I}, observed with XAS and UV-vis spectroscopy, with the evolvement of the CO_2 and CH_4 MS fragments, we found an unambiguous connection between the three traces. Additionally, a small but consistent difference was observed between the two different MOR compositions. The 018Cu-MOR(7) sample, with the highest methane activity in MTM[18] as well as the highest abundance of **Cu^{II}_HT_b** after pre-treatment, showed a faster reduction at low temperatures compared to 036Cu-MOR(11) (see Scheme 2b). This observation offers an additional piece of evidence in connecting the **Cu^{II}_HT_b**, described as a mono-μ-oxo dicopper(II) core with Cu–Cu internuclear separation around 3 Å, with the MTM active site in the investigated Cu-MOR samples.

Notably, *in situ* UV-vis during CH_4-TPR evidenced the evolution of a complex "multiplet" band in the d–d region of 036Cu-MOR(11). This band, previously observed in Cu-CHA[75,76] and reported here for the first time in Cu-MOR, was loosely assigned to a high-temperature, three-fold coordinated Cu^{II} species, much more abundant in 036Cu-MOR(11) and thus likely related to the **Cu^{II}_HT_a** component.

5 Conclusions

In this work, detailed insight into the dynamic changes of the Cu-speciation during light alkane selective oxidation has been obtained. We collected *in situ* XAS spectra on two compositionally different Cu-MOR zeolites during temperature programmed reduction experiments with CH_4, C_2H_6, and CO. Upon coupling the relevant MS traces with MCR-ALS analysis of the XANES data, we reveal clear behavioral differences among the reducing agents and trends related both to local structure and Cu reducibility. The relevant experimental conditions allowed us to connect reducibility to the MTM activity for mordenites, which has previously been dubious due to "self-reduction" resistant Cu species in the highly active sample, 018Cu-MOR(7). Additional *in situ* UV-vis and FT-IR spectroscopy experiments allowed for confirmative and additional information related to the Cu-speciation. We also applied a leading-edge method using the MCR-ALS derived spectra to extract EXAFS signals for all pure Cu species. Wavelet transform (WT) analysis on the pure EXAFS spectra provided confirmative information on Cu–Cu single scattering contributions in the 3.0–3.5 Å^{-1} interatomic distance range for all three Cu^{II} species, which confirmed the hypothesis of these species being related to dimeric copper species. This study has pushed the boundaries for how MCR-ALS analysis and EXAFS-WT mapping can be used. We anticipate that the experimental procedure and data analysis strategy presented herein, especially when combined with complementary techniques like UV-vis and FT-IR spectroscopy, will have great impact on our understanding of other systems. In particular, we anticipate that such research will be very important in the advancing our understanding of other transition metal loaded zeolites in selective oxidation, and also to shed further light on the reactivity of substrates other than methane. Finally, the approach can further be transferred to many other reactions where the complex superimposition of various phenomena has led to inconclusive results thus far.

Data availability

ESI† is available in the additional files and further supporting data is available from the authors upon request.

Author contributions

K. K.: conceptualization, investigation, formal analysis, writing – original draft, visualization. B. G.: investigation, formal analysis, writing – original draft, visualization. M. S., B. G. S., G. D., S. P.: investigation, writing – review & editing. U. O., P. B., S. B.: supervision, validation, writing – review & editing. S. S.: conceptualization, supervision, funding acquisition, writing – review & editing. E. B.: formal analysis, methodology, writing – original draft, supervision.

Conflicts of interest

There are no conflicts to declare.

Acknowledgements

The authors acknowledge the iCSI (industrial Catalysis Science and Innovation) Centre for Research-based Innovation, which receives financial support from the Research Council of Norway under contract no. 237922. The authors also acknowledge funding from Horizon 2020 Excellence Science ERC-Synergy program 2019-CUBE: "Unravelling the secrets of Cu-based catalysts for C–H activation" (grant agreement no. 856446). B. G., G. D., M. S., S. B. and E. B. acknowledge support from the Project CH4.0 under the MUR program "Dipartimenti di Eccellenza 2023-2027" (CUP: D13C22003520001). We acknowledge the European Synchrotron Radiation Facility (ESRF) for the provision of synchrotron radiation facilities, and we would like to thank W. van Beek, D. Stoian, and K. Marshall for assistance and support in using beamline BM31. We also would like to acknowledge MAX IV Laboratory for time on Beamline Balder under Proposal 20190347, which laid the foundation for developing the experiment performed at BM31. Research conducted at MAX IV, a Swedish national user facility, is supported by the Swedish Research Council under contract 2018–07152, the Swedish Governmental Agency for Innovation Systems under contract 2018-04969, and Formas under contract 2019-02496. We thank the staff, J. Just, M. Ciambezi, and K. Klementiev for help and guidance at the beamline. We are grateful to A. Martini for programming and making available the script employed for WT-EXAFS analysis and to D. K. Pappas for the initial conceptualization of the TPR-XAS study as well as contribution to our background knowledge on the investigated systems.

References

1 J. H. Lunsford, Catalytic conversion of methane to more useful chemicals and fuels: a challenge for the 21st century, *Catal. Today*, 2000, **63**, 165–174.

2 R. Horn and R. Schlögl, Methane Activation by Heterogeneous Catalysis, *Catal. Lett.*, 2015, **145**, 23–39.

3 M. Ravi, M. Ranocchiari and J. A. van Bokhoven, The Direct Catalytic Oxidation of Methane to Methanol-A Critical Assessment, *Angew. Chem., Int. Ed.*, 2017, **56**, 16464–16483.

4 M. H. Groothaert, P. J. Smeets, B. F. Sels, P. A. Jacobs and R. A. Schoonheydt, Selective oxidation of methane by the bis(μ-oxo)dicopper core stabilized on ZSM-5 and mordenite zeolites, *J. Am. Chem. Soc.*, 2005, **127**, 1394–1395.

5 A. A. Latimer, A. Kakekhani, A. R. Kulkarni and J. K. Nørskov, Direct Methane to Methanol: The Selectivity–Conversion Limit and Design Strategies, *ACS Catal.*, 2018, **8**, 6894–6907.

6 V. L. Sushkevich, D. Palagin, M. Ranocchiari and J. A. van Bokhoven, Selective Anaerobic Oxidation of Methane Enables Direct Synthesis of Methanol, *Science*, 2017, **356**, 523–527.

7 E. M. Alayon, M. Nachtegaal, M. Ranocchiari and J. A. van Bokhoven, Catalytic conversion of methane to methanol over Cu-mordenite, *Chem. Commun.*, 2012, **48**, 404–406.

8 S. Grundner, W. Luo, M. Sanchez-Sanchez and J. A. Lercher, Synthesis of Single-Site Copper Catalysts for Methane Partial Oxidation, *Chem. Commun.*, 2016, **52**, 2553–2556.

9 P. Tomkins, A. Mansouri, S. E. Bozbag, F. Krumeich, M. B. Park, E. M. Alayon, M. Ranocchiari and J. A. van Bokhoven, Isothermal Cyclic Conversion of Methane into Methanol over Copper-Exchanged Zeolite at Low Temperature, *Angew. Chem., Int. Ed.*, 2016, **55**, 5467–5471.

10 S. Prodinger, K. Kvande, B. Arstad, E. Borfecchia, P. Beato and S. Svelle, Synthesis–Structure–Activity Relationship in Cu-MOR for Partial Methane Oxidation: Al Siting via Inorganic Structure-Directing Agents, *ACS Catal.*, 2022, **12**, 2166–2177.

11 S. Grundner, M. A. C. Markovits, G. Li, M. Tromp, E. A. Pidko, E. J. M. Hensen, A. Jentys, M. Sanchez-Sanchez and J. A. Lercher, Single-site trinuclear copper oxygen clusters in mordenite for selective conversion of methane to methanol, *Nat. Commun.*, 2015, **6**, 7546.

12 D. K. Pappas, E. Borfecchia, M. Dyballa, I. A. Pankin, K. A. Lomachenko, A. Martini, M. Signorile, S. Teketel, B. Arstad, G. Berlier, C. Lamberti, S. Bordiga, U. Olsbye, K. P. Lillerud, S. Svelle and P. Beato, Methane to Methanol: Structure-Activity Relationships for Cu-CHA, *J. Am. Chem. Soc.*, 2017, **139**, 14961–14975.

13 M. J. Wulfers, S. Teketel, B. Ipek and R. F. Lobo, Conversion of Methane to Methanol on Copper-Containing Small-Pore Zeolites and Zeotypes, *Chem. Commun.*, 2015, **51**, 4447–4450.

14 D. K. Pappas, E. Borfecchia, M. Dyballa, K. A. Lomachenko, A. Martini, G. Berlier, B. Arstad, C. Lamberti, S. Bordiga, U. Olsbye, S. Svelle and P. Beato, Understanding and Optimizing the Performance of Cu-FER for The Direct CH_4 to CH_3OH Conversion, *ChemCatChem*, 2019, **11**, 621–627.

15 V. L. Sushkevich and J. A. van Bokhoven, Methane-to-Methanol: Activity Descriptors in Copper-Exchanged Zeolites for the Rational Design of Materials, *ACS Catal.*, 2019, **9**, 6293–6304.

16 A. J. Knorpp, A. B. Pinar, M. A. Newton, V. L. Sushkevich and J. A. van Bokhoven, Copper-Exchanged Omega (MAZ) Zeolite: Copper-Concentration Dependent Active Sites and its Unprecedented Methane to Methanol Conversion, *ChemCatChem*, 2018, **10**, 5593–5596.

17 K. Kvande, S. Prodinger, F. Schlimpen, P. Beato, P. Pale, S. Chassaing and S. Svelle, Copper-zeolites Prepared by

Solid-state Ion Exchange - Characterization and Evaluation for the Direct Conversion of Methane to Methanol, *Top. Catal.*, 2022, DOI: **10.1007/s11244-022-01763-7**.

18 D. K. Pappas, A. Martini, M. Dyballa, K. Kvande, S. Teketel, K. A. Lomachenko, R. Baran, P. Glatzel, B. Arstad, G. Berlier, C. Lamberti, S. Bordiga, U. Olsbye, S. Svelle, P. Beato and E. Borfecchia, The Nuclearity of the Active Site for Methane to Methanol Conversion in Cu-Mordenite: A Quantitative Assessment, *J. Am. Chem. Soc.*, 2018, **140**, 15270–15278.

19 K. Kvande, D. K. Pappas, E. Borfecchia and K. A. Lomachenko, Advanced X-ray Absorption Spectroscopy Analysis to Determine Structure-Activity Relationships for Cu-Zeolites in the Direct Conversion of Methane to Methanol, *ChemCatChem*, 2020, **12**, 2385–2405.

20 V. L. Sushkevich, M. Artsiusheuski, D. Klose, G. Jeschke and J. A. van Bokhoven, Identification of Kinetic and Spectroscopic Signatures of Copper Sites for Direct Oxidation of Methane to Methanol, *Angew. Chem., Int. Ed.*, 2021, **60**, 15944–15953.

21 M. A. Newton, A. J. Knorpp, A. B. Pinar, V. L. Sushkevich, D. Palagin and J. A. van Bokhoven, On the Mechanism Underlying the Direct Conversion of Methane to Methanol by Copper Hosted in Zeolites; Braiding Cu K-Edge XANES and Reactivity Studies, *J. Am. Chem. Soc.*, 2018, **140**, 10090–10093.

22 J. Zheng, I. Lee, E. Khramenkova, M. Wang, B. Peng, O. Y. Gutierrez, J. L. Fulton, D. M. Camaioni, R. Khare, A. Jentys, G. L. Haller, E. A. Pidko, M. Sanchez-Sanchez and J. A. Lercher, Importance of Methane Chemical Potential for Its Conversion to Methanol on Cu-Exchanged Mordenite, *Chem.–Eur. J.*, 2020, **26**, 7563–7567.

23 K. A. Lomachenko, A. Martini, D. K. Pappas, C. Negri, M. Dyballa, G. Berlier, S. Bordiga, C. Lamberti, U. Olsbye, S. Svelle, P. Beato and E. Borfecchia, The impact of reaction conditions and material composition on the stepwise methane to methanol conversion over Cu-MOR: an operando XAS study, *Catal. Today*, 2019, **336**, 99–108.

24 D. Plessers, A. J. Heyer, H. M. Rhoda, M. L. Bols, E. I. Solomon, R. A. Schoonheydt and B. F. Sels, Tuning Copper Active Site Composition in Cu-MOR through Co-Cation Modification for Methane Activation, *ACS Catal.*, 2023, **13**, 1906–1915.

25 M. Dyballa, K. Thorshaug, D. K. Pappas, E. Borfecchia, K. Kvande, S. Bordiga, G. Berlier, A. Lazzarini, U. Olsbye, P. Beato, S. Svelle and B. Arstad, Zeolite Surface Methoxy Groups as Key Intermediates in the Stepwise Conversion of Methane to Methanol, *ChemCatChem*, 2019, **11**, 5022–5026.

26 V. L. Sushkevich, J. A. van Bokhoven and R. Verel, Pathways of Methane Transformation over Copper-Exchanged Mordenite as Revealed by In Situ NMR and IR Spectroscopy, *Angew. Chem., Int. Ed.*, 2020, **59**, 910–918.

27 L. Sun, Y. Wang, C. Wang, Z. Xie, N. Guan and L. Li, Water-involved methane-selective catalytic oxidation by dioxygen over copper zeolites, *Chem*, 2021, **7**, 1557–1568.

28 A. Koishybay and D. F. Shantz, Water Is the Oxygen Source for Methanol Produced in Partial Oxidation of Methane in a Flow Reactor over Cu-SSZ-13, *J. Am. Chem. Soc.*, 2020, **142**, 11962–11966.

29 X. Liu, T. Liang, R. Barbosa, G. Chen, H. Toghiani and Y. Xiang, Ammoxidation of Ethane to Acetonitrile and Ethylene: Reaction Transient Analysis for the Co/HZSM-5 Catalyst, *ACS Omega*, 2020, **5**, 1669–1678.

30 M. A. Newton, A. J. Knorpp, V. L. Sushkevich, D. Palagin and J. A. van Bokhoven, Active sites and mechanisms in the direct conversion of methane to methanol using Cu in zeolitic hosts: a critical examination, *Chem. Soc. Rev.*, 2020, **49**, 1449–1486.

31 K. Kvande, D. K. Pappas, M. Dyballa, C. Buono, M. Signorile, E. Borfecchia, K. A. Lomachenko, B. Arstad, S. Bordiga, G. Berlier, U. Olsbye, P. Beato and S. Svelle, Comparing the Nature of Active Sites in Cu-loaded SAPO-34 and SSZ-13 for the Direct Conversion of Methane to Methanol, *Catalysts*, 2020, **10**, 191.

32 D. K. Pappas, K. Kvande, M. Kalyva, M. Dyballa, K. A. Lomachenko, B. Arstad, E. Borfecchia, S. Bordiga, U. Olsbye, P. Beato and S. Svelle, Influence of Cu-speciation in mordenite on direct methane to methanol conversion: Multi-Technique characterization and comparison with NH3 selective catalytic reduction of NOx, *Catal. Today*, 2021, **369**, 105–111.

33 M. Dyballa, D. K. Pappas, K. Kvande, E. Borfecchia, B. Arstad, P. Beato, U. Olsbye and S. Svelle, On How Copper Mordenite Properties Govern the Framework Stability and Activity in the Methane-to-Methanol Conversion, *ACS Catal.*, 2019, **9**, 365–375.

34 A. Martini, M. Signorile, C. Negri, K. Kvande, K. A. Lomachenko, S. Svelle, P. Beato, G. Berlier, E. Borfecchia and S. Bordiga, EXAFS wavelet transform analysis of Cu-MOR zeolites for the direct methane to methanol conversion, *Phys. Chem. Chem. Phys.*, 2020, **22**, 18950–18963.

35 A. Martini, E. Borfecchia, K. A. Lomachenko, I. A. Pankin, C. Negri, G. Berlier, P. Beato, H. Falsig, S. Bordiga and C. Lamberti, Composition-Driven Cu-Speciation and Reducibility in Cu-CHA Zeolite Catalysts: a Multivariate XAS/FTIR Approach to Complexity, *Chem. Sci.*, 2017, **8**, 6836–6851.

36 A. Martini, E. Alladio and E. Borfecchia, Determining Cu–Speciation in the Cu–CHA Zeolite Catalyst: The Potential of Multivariate Curve Resolution Analysis of In Situ XAS Data, *Top. Catal.*, 2018, **61**, 1396–1407.

37 J. S. Valente, R. Quintana-Solórzano, H. Armendáriz-Herrera and J.-M. M. Millet, Decarbonizing Petrochemical Processes: Contribution and Perspectives of the Selective Oxidation of C1–C3 Paraffins, *ACS Catal.*, 2023, **13**, 1693–1716.

38 K. I. Hadjiivanov, M. M. Kantcheva and D. G. Klissurski, IR study of CO adsorption on Cu-ZSM-5 and CuO/SiO2 catalysts: σ and π components of the Cu+—CO bond, *J. Chem. Soc., Faraday Trans.*, 1996, **92**, 4595–4600.

39 V. M. Rakić, R. V. Hercigonja and V. T. Dondur, CO interaction with zeolites studied by TPD and FTIR: transition-metal ion-exchanged FAU-type zeolites, *Microporous Mesoporous Mater.*, 1999, **27**, 27–39.

40 G. Deplano, M. Signorile, V. Crocellà, N. G. Porcaro, C. Atzori, B. G. Solemsli, S. Svelle and S. Bordiga, Titration of Cu(I) Sites in Cu-ZSM-5 by Volumetric CO Adsorption, *ACS Appl. Mater. Interfaces*, 2022, **14**, 21059–21068.

41 R. Bulánek, B. Wichterlová, Z. Sobalík and J. Tichý, Reducibility and oxidation activity of Cu ions in zeolites - Effect of Cu ion coordination and zeolite framework composition, *Appl. Catal. B Environ.*, 2001, **31**, 13–25.

42 H. Li, C. Paolucci, I. Khurana, L. N. Wilcox, F. Göltl, J. D. Albarracin-Caballero, A. J. Shih, F. H. Ribeiro, R. Gounder and W. F. Schneider, Consequences of exchange-site heterogeneity and dynamics on the UV-visible spectrum of Cu-exchanged SSZ-13, *Chem. Sci.*, 2019, **10**, 2373–2384.

43 R. Villamaina, U. Iacobone, I. Nova, M. P. Ruggeri, J. Collier, D. Thompsett and E. Tronconi, Low-T CO Oxidation over Cu−CHA Catalysts in Presence of NH3: Probing the Mobility of CuII Ions and the Role of Multinuclear CuII Species, *ChemCatChem*, 2020, **12**, 3843–3848.

44 P. Da Costa, B. Modén, G. D. Meitzner, D. K. Lee and E. Iglesia, Spectroscopic and chemical characterization of active and inactive Cu species in NO decomposition catalysts based on Cu-ZSM5, *Phys. Chem. Chem. Phys.*, 2002, **4**, 4590–4601.

45 W. H. Cassinelli, L. Martins, A. R. Passos, S. H. Pulcinelli, C. V. Santilli, A. Rochet and V. Briois, Multivariate curve resolution analysis applied to time-resolved synchrotron X-ray Absorption Spectroscopy monitoring of the activation of copper alumina catalyst, *Catal. Today*, 2014, **229**, 114–122.

46 E. Borfecchia, D. K. Pappas, M. Dyballa, K. A. Lomachenko, C. Negri, M. Signorile and G. Berlier, Evolution of Active Sites During Selective Oxidation of Methane to Methanol over Cu-CHA and Cu-MOR Zeolites as Monitored by Operando XAS, *Catal. Today*, 2019, **333**, 17–27.

47 P. M. Abdala, O. V. Safonova, G. Wiker, W. van Beek, H. Emerich, J. A. van Bokhoven, J. Sa, J. Szlachetko and M. Nachtegaal, Scientific Opportunities for Heterogeneous Catalysis Research at the SuperXAS and SNBL Beam Lines, *Chimia*, 2012, **66**, 699–705.

48 W. van Beek, O. V. Safonova, G. Wiker and H. Emerich, SNBL, a dedicated beamline for combined in situ X-ray diffraction, X-ray absorption and Raman scattering experiments, *Phase Transitions*, 2011, **84**, 726–732.

49 B. Ravel and M. Newville, ATHENA, ARTEMIS, HEPHAESTUS: data analysis for X-ray absorption spectroscopy using IFEFFIT, *J. Synchrotron Radiat.*, 2005, **12**, 537–541.

50 J. E. Penner-Hahn, X-ray absorption spectroscopy in coordination chemistry, *Coord. Chem. Rev.*, 1999, **190**, 1101–1123.

51 S. Bordiga, E. Groppo, G. Agostini, J. A. van Bokhoven and C. Lamberti, Reactivity of Surface Species in Heterogeneous Catalysts Probed by In Situ X-ray Absorption Techniques, *Chem. Rev.*, 2013, **113**, 1736–1850.

52 C. Ruckebusch, *Resolving spectral mixtures: with applications from ultrafast time-resolved spectroscopy to super-resolution imaging*, Elsevier, 2016.

53 C. Ruckebusch and L. Blanchet, Multivariate curve resolution: a review of advanced and tailored applications and challenges, *Anal. Chim. Acta*, 2013, **765**, 28–36.

54 A. de Juan and R. Tauler, Chemometrics applied to unravel multicomponent processes and mixtures: revisiting latest trends in multivariate resolution, *Anal. Chim. Acta*, 2003, **500**, 195–210.

55 W. Windig and J. Guilment, Interactive self-modeling mixture analysis, *Anal. Chem.*, 1991, **63**, 1425–1432.

56 J. Jaumot, R. Gargallo, A. De Juan and R. Tauler, A graphical user-friendly interface for MCR-ALS: a new tool for multivariate curve resolution in MATLAB, *Chemom. Intell. Lab. Syst.*, 2005, **76**, 101–110.

57 H. Funke, A. C. Scheinost and M. Chukalina, Wavelet Analysis of Extended X-Ray Absorption Fine Structure Data, *Phys. Rev. B: Condens. Matter Mater. Phys.*, 2005, **71**, 094110.

58 M. Muñoz, P. Argoul and F. Farges, Continuous Cauchy wavelet transform analyses of EXAFS spectra: a qualitative approach, *Am. Mineral.*, 2003, **88**, 694–700.

59 J. Timoshenko and A. Kuzmin, Wavelet Data Analysis of EXAFS Spectra, *Comput. Phys. Commun.*, 2009, **180**, 920–925.

60 I. A. Pankin, A. Martini, K. A. Lomachenko, A. V. Soldatov, S. Bordiga and E. Borfecchia, Identifying Cu-Oxo Species In Cu-Zeolites By XAS: A Theoretical Survey by DFT-Assisted XANES Simulation and EXAFS Wavelet Transform, *Catal. Today*, 2020, **345**, 125–135.

61 V. L. Sushkevich, O. V. Safonova, D. Palagin, M. A. Newton and J. A. van Bokhoven, Structure of Copper Sites in Zeolites Examined by Fourier and Wavelet Transform Analysis of EXAFS, *Chem. Sci.*, 2020, **11**, 5299–5312.

62 T. J. Penfold, I. Tavernelli, C. J. Milne, M. Reinhard, A. El Nahhas, R. Abela, U. Rothlisberger and M. Chergui, A wavelet analysis for the X-ray absorption spectra of molecules, *J. Chem. Phys.*, 2013, **138**, 014104.

63 B. E. R. Snyder, P. Vanelderen, R. A. Schoonheydt, B. F. Sels and E. I. Solomon, Second-Sphere Effects on Methane Hydroxylation in Cu-Zeolites, *J. Am. Chem. Soc.*, 2018, **140**, 9236–9243.

64 P. Vanelderen, B. E. R. Snyder, M.-L. Tsai, R. G. Hadt, J. Vancauwenbergh, O. Coussens, R. A. Schoonheydt, B. F. Sels and E. I. Solomon, Spectroscopic definition of the copper active sites in mordenite: selective methane oxidation, *J. Am. Chem. Soc.*, 2015, **137**, 6383–6392.

65 H. Funke, M. Chukalina and A. C. Scheinost, A new FEFF-based wavelet for EXAFS data analysis, *J. Synchrotron Radiat.*, 2007, **14**, 426–432.

66 I. A. Pankin, H. I. Hamoud, K. A. Lomachenko, S. B. Rasmussen, A. Martini, P. Bazin, V. Valtchev, M. Daturi, C. Lamberti and S. Bordiga, Cu-and Fe-speciation in a composite zeolite catalyst for selective catalytic reduction of NOx: insights from operando XAS, *Catal. Sci. Technol.*, 2021, **11**, 846–860.

67 G. Brezicki, J. D. Kammert, T. B. Gunnoe, C. Paolucci and R. J. Davis, Insights into the Speciation of Cu in the Cu-H-Mordenite Catalyst for the Oxidation of Methane to Methanol, *ACS Catal.*, 2019, **9**, 5308–5319.

68 A. Voronov, A. Urakawa, W. van Beek, N. E. Tsakoumis, H. Emerich and M. Ronning, Multivariate curve resolution applied to in situ X-ray absorption spectroscopy data: an efficient tool for data processing and analysis, *Anal. Chim. Acta*, 2014, **840**, 20–27.

69 A. Martini and E. Borfecchia, Spectral Decomposition of X-ray Absorption Spectroscopy Datasets: Methods and Applications, *Crystals*, 2020, **10**, 664.

70 C. Buono, A. Martini, I. A. Pankin, D. K. Pappas, C. Negri, K. Kvande, K. A. Lomachenko and E. Borfecchia, Local structure of Cu(I) ions in the MOR zeolite: A DFT-assisted XAS study, *Radiat. Phys. Chem.*, 2020, **175**, 108111.

71 B. Ruscic, Active Thermochemical Tables: Sequential Bond Dissociation Enthalpies of Methane, Ethane, and Methanol and the Related Thermochemistry, *J. Phys. Chem. A*, 2015, **119**, 7810–7837.

72 P. J. Smeets, R. G. Hadt, J. S. Woertink, P. Vanelderen, R. A. Schoonheydt, B. F. Sels and E. I. Solomon, Oxygen Precursor to the Reactive Intermediate in Methanol Synthesis by Cu-ZSM-5, *J. Am. Chem. Soc.*, 2010, **132**, 14736–14738.

73 J. Hunt, A. Ferrari, A. Lita, M. Crosswhite, B. Ashley and A. E. Stiegman, Microwave-Specific Enhancement of the Carbon–Carbon Dioxide (Boudouard) Reaction, *J. Phys. Chem. C*, 2013, **117**, 26871–26880.

74 P. J. Smeets, M. H. Groothaert and R. A. Schoonheydt, Cu Based Zeolites: A UV-Vis Study of the Active Site in the Selective Methane Oxidation at Low Temperatures, *Catal. Today*, 2005, **110**, 303–309.

75 F. Giordanino, P. N. R. Vennestrom, L. F. Lundegaard, F. N. Stappen, S. Mossin, P. Beato, S. Bordiga and C. Lamberti, Characterization of Cu-Exchanged SSZ-13: a Comparative FTIR, UV-Vis, and EPR Study with Cu-ZSM-5 and Cu-beta with Similar Si/Al and Cu/Al Ratios, *Dalton Trans.*, 2013, **42**, 12741–12761.

76 C. Negri, T. Selleri, E. Borfecchia, A. Martini, K. A. Lomachenko, T. V. W. Janssens, M. Cutini, S. Bordiga and G. Berlier, Structure and Reactivity of Oxygen-Bridged Diamino Dicopper(II) Complexes in Cu-Ion-Exchanged Chabazite Catalyst for NH3-Mediated Selective Catalytic Reduction, *J. Am. Chem. Soc.*, 2020, **142**, 15884–15896.

77 G. T. Palomino, P. Fisicaro, S. Bordiga, A. Zecchina, E. Giamello and C. Lamberti, Oxidation states of copper ions in ZSM-5 zeolites. A multitechnique investigation, *J. Phys. Chem. B*, 2000, **104**, 4064–4073.

78 G. Brezicki, J. Zheng, C. Paolucci, R. Schlögl and R. J. Davis, Effect of the Co-cation on Cu Speciation in Cu-Exchanged Mordenite and ZSM-5 Catalysts for the Oxidation of Methane to Methanol, *ACS Catal.*, 2021, **11**, 4973–4987.

79 C. Lamberti, S. Bordiga, M. Salvalaggio, G. Spoto, A. Zecchina, F. Geobaldo, G. Vlaic and M. Bellatreccia, XAFS, IR, and UV-Vis Study of the Cu^{I} Environment in Cu^{I}-ZSM-5, *J. Phys. Chem. B*, 1997, **101**, 344–360.

80 G. Deplano, A. Martini, M. Signorile, E. Borfecchia, V. Crocellà, S. Svelle and S. Bordiga, Copper Pairing in the Mordenite Framework as a Function of the Cu^{I}/Cu^{II} Speciation, *Angew. Chem., Int. Ed.*, 2021, **60**, 25891–25896.

81 S. Bordiga, C. Lamberti, F. Bonino, A. Travert and F. Thibault-Starzyk, Probing zeolites by vibrational spectroscopies, *Chem. Soc. Rev.*, 2015, **44**, 7262–7341.

82 U. Iacobone, I. Nova, E. Tronconi, R. Villamaina, M. P. Ruggeri, J. Collier and D. Thompsett, Appraising Multinuclear Cu2+ Structure Formation in Cu-CHA SCR Catalysts via Low-T Dry CO Oxidation with Modulated NH3 Solvation, *ChemistryOpen*, 2022, **11**, e202200186.

83 E. Borfecchia, P. Beato, S. Svelle, U. Olsbye, C. Lamberti and S. Bordiga, Cu-CHA – a model system for applied selective redox catalysis, *Chem. Soc. Rev.*, 2018, **47**, 8097–8133.

84 M. A. Artsiusheuski, J. A. van Bokhoven and V. L. Sushkevich, Structure of Selective and Nonselective Dicopper (II) Sites in CuMFI for Methane Oxidation to Methanol, *ACS Catal.*, 2022, **12**, 15626–15637.

85 L. Vilella and F. Studt, The Stability of Copper Oxo Species in Zeolite Frameworks, *Eur. J. Inorg. Chem.*, 2016, **2016**, 1514–1520.

86 V. L. Sushkevich, D. Palagin and J. A. van Bokhoven, The Effect of the Active-Site Structure on the Activity of Copper Mordenite in the Aerobic and Anaerobic Conversion of Methane into Methanol, *Angew. Chem., Int. Ed.*, 2018, **57**, 8906–8910.

87 R. Haase, T. Beschnitt, U. Flörke and S. Herres-Pawlis, Bidentate guanidine ligands with ethylene spacer in copper-dioxygen chemistry: Structural characterization of bis(μ-hydroxo) dicopper complexes, *Inorg. Chim. Acta*, 2011, **374**, 546–557.

88 M. R. Halvagar, P. V. Solntsev, H. Lim, B. Hedman, K. O. Hodgson, E. I. Solomon, C. J. Cramer and W. B. Tolman, Hydroxo-Bridged Dicopper(II,III) and -(III,III) Complexes: Models for Putative Intermediates in Oxidation Catalysis, *J. Am. Chem. Soc.*, 2014, **136**, 7269–7272.

89 G. Li, P. Vassilev, M. Sanchez-Sanchez, J. A. Lercher, E. J. M. Hensen and E. A. Pidko, Stability and reactivity of copper oxo-clusters in ZSM-5 zeolite for selective methane oxidation to methanol, *J. Catal.*, 2016, **338**, 305–312.

90 F. Göltl, S. Bhandari and M. Mavrikakis, Thermodynamics Perspective on the Stepwise Conversion of Methane to Methanol over Cu-Exchanged SSZ-13, *ACS Catal.*, 2021, **11**, 7719–7734.

91 L. Tao, I. Lee, R. Khare, A. Jentys, J. L. Fulton, M. Sanchez-Sanchez and J. A. Lercher, Speciation of Cu-Oxo Clusters in Ferrierite for Selective Oxidation of Methane to Methanol, *Chem. Mater.*, 2022, **34**, 4355–4363.

92 M. A. Artsiusheuski, O. Safonova, D. Palagin, J. A. van Bokhoven and V. L. Sushkevich, Structural Evolution of Copper-Oxo Sites in Zeolites upon the Reaction with Methane Investigated by Means of Cu K-edge X-ray Absorption Spectroscopy, *J. Phys. Chem. C*, 2023, **127**, 9603–9615.

93 K. Kvande, S. Prodinger, B. G. Solemsli, S. Bordiga, E. Borfecchia, U. Olsbye, P. Beato and S. Svelle, Cu-loaded zeolites enable the selective activation of ethane to ethylene at low temperatures and pressure, *Chem. Commun.*, 2023, **59**, 6052–6055.